Provided for non-commercial research and education use.
Not for reproduction, distribution or commercial use.

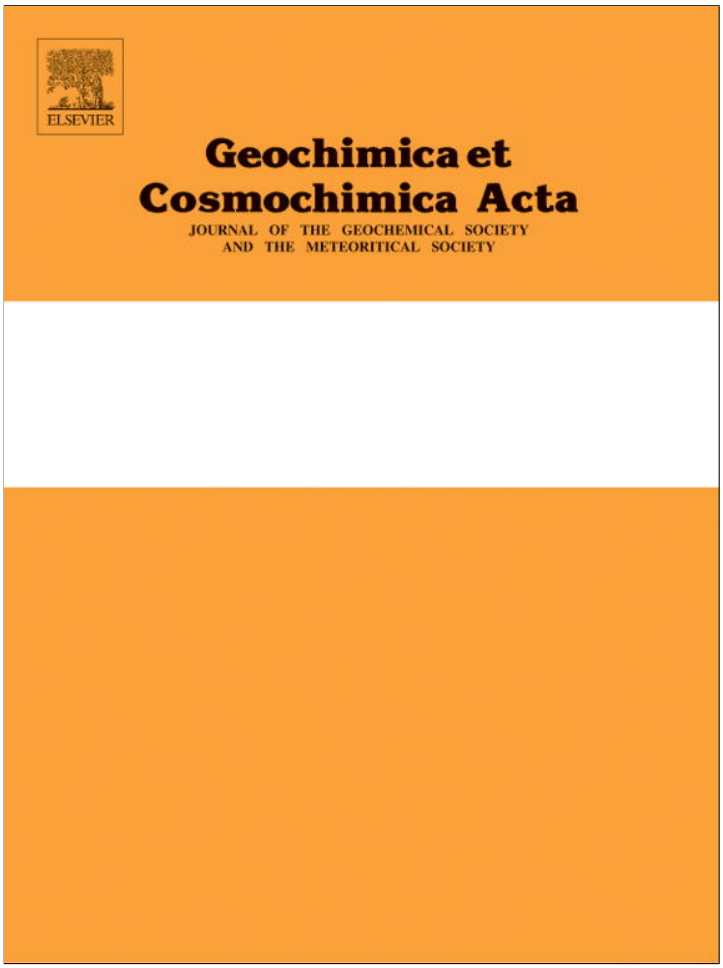


This article appeared in a journal published by Elsevier. The attached copy is furnished to the author for internal non-commercial research and education use, including for instruction at the authors institution and sharing with colleagues.

Other uses, including reproduction and distribution, or selling or licensing copies, or posting to personal, institutional or third party websites are prohibited.

In most cases authors are permitted to post their version of the article (e.g. in Word or Tex form) to their personal website or institutional repository. Authors requiring further information regarding Elsevier's archiving and manuscript policies are encouraged to visit:

http://www.elsevier.com/authorsrights

Author's personal copy

Available online at www.sciencedirect.com

SciVerse ScienceDirect

Geochimica et Cosmochimica Acta 110 (2013) 152–175

Geochimica et Cosmochimica Acta

www.elsevier.com/locate/gca

# SIMS Pb–Pb and U–Pb age determination of eucrite zircons at $< 5$ μm scale and the first 50 Ma of the thermal history of Vesta

Qin Zhou [a,1], Qing-Zhu Yin [b,*,1], Edward D. Young [c], Xian-Hua Li [a], Fu-Yuan Wu [a], Qiu-Li Li [a], Yu Liu [a], Guo-Qiang Tang [a]

[a] State Key Laboratory of Lithospheric Evolution, Institute of Geology and Geophysics, Chinese Academy of Sciences, Beijing 100029, China
[b] Department of Geology, University of California at Davis, One Shields Avenue, Davis, CA 95616, USA
[c] Department of Earth and Space Sciences and the Institute of Geophysics and Planetary Physics, University of California Los Angeles, 595 Charles E. Young Drive East, Los Angeles, CA 90095, USA

Received 31 July 2011; accepted in revised form 11 February 2013; Available online 27 February 2013

**Abstract**

Eucrites, a subgroup of basaltic achondrites, represent the remnants of the earliest magmatic stage of the Solar System formation, possibly on the asteroid 4 Vesta. The precise determination of their crystallization age is therefore important for constraining the evolutionary history of the asteroid, including melting and differentiation processes of the parent body. Zircons would be the best mineral for such purpose. However, extra-terrestrial zircons are rare, and those found in eucrites are typically small (<5 μm). Using a Cameca IMS-1280 high-resolution ion microprobe, precise uranium–lead (U–Pb) and Pb–Pb ages of the non-cumulate basaltic eucrite zircons in Béréba, Cachari, Caldera, Camel Donga, and Juvinas were determined successfully at scale of $< 5$ μm. We obtained a weighted average $^{207}Pb/^{206}Pb$ age of $4541 \pm 11$ Ma and U–Pb concordia age of $4525 \pm 24$ Ma for the five eucrite samples studied. A synthesis of available age data of howardites, eucrites and diogenites indicate a protracted magmatic history on Vesta, with a most pronounced core–mantle differentiation event marked at $4564 \pm 2$ Ma, followed by a peak of basaltic magmatism at $4552 \pm 7$ Ma, which gradually diminished over the next 50 Ma. Thermal modeling of Vesta suggests that partial melt fraction of greater than 10%, with temperature well exceeding 1500 K could be maintained over this period throughout its interior. This is consistent with the chronological records of eucrites suggesting persistent magmatism on Vesta during the first 50 Ma in the early Solar System.
© 2013 Elsevier Ltd. All rights reserved.

## 1. INTRODUCTION

Eucrites, a member of HED (howardite, eucrite and dioggenite) family, belongs to subgroup of basaltic achondrites representing one of the earliest planetary igneous activities of a differentiated parent body, possibly the asteroid 4 Vesta (Binzel and Xu, 1993; Drake, 2001). As planetary accretion proceeds from small to increasingly larger bodies, igneous processes are the primary means by which planetary bodies evolve and differentiate from their initial composition to one with distinct concentric layers of core, mantle and crust. Thus, meteorites such as eucrites provide one of the most important windows into the early evolutionary history of evolved planetesimals. The age of the igneous event that generated basaltic eucrites is of primary importance, since this information can be used to constrain the evolutionary history, including melting and differentiation processes of the parent body. Our understanding of the eucrite-Vesta connection has improved substantially, as NASA's Dawn mission has successfully completed orbiting Vesta from July 2011 to September 2012. The mission has provided rich dataset of mapping, crater count age, mineralogy, temperature, geochemistry, topography, gravity, and photometry to shed light on the origin, evolution, structure, geology and surface composition of Vesta (e.g.

* Corresponding author.
*E-mail address:* qyin@ucdavis.edu (Q.-Z. Yin).
[1] These authors contributed equally to this work.

0016-7037/$ - see front matter © 2013 Elsevier Ltd. All rights reserved.
http://dx.doi.org/10.1016/j.gca.2013.02.016

Author's personal copy



Russell et al., 2012). Improving chronological information of basaltic eucrites in our collection, and strengthening meteorite connections with the basaltic flood plain on the surface of Vesta with higher resolution images returned from Dawn Mission are timely and highly desirable.

Acquiring precise and accurate formation ages and piecing together thermal histories for eucrites is complicated by complex post-crystallization events such as impact heating and remelting (Fredriksson and Kraut, 1967; Buchanan et al., 2005). Such events reset the isotopic systems in eucrites to various degrees, resulting in inconsistent age data among both short-lived and long-lived isotopic systems, depending on the mineral susceptibilities to such disturbances, and the closure temperature of these isotopic systems (Bogard et al., 1985; Bogard, 1995; Shukolyukov and Begemann, 1996a; Tera et al., 1997). The U–Pb isotopic system of U-bearing accessory minerals, (e.g., zircon, baddeleyite and zirconolite) is less affected by post-crystallization events and is widely regarded as the best means of dating primary, or early, magmatic events (Misawa et al., 2005; Chamberlain et al., 2010; Schmitt et al., 2010; Wu et al., 2010).

Although zirconium-bearing minerals are rare in most planetary material due to typically low zirconium concentrations (Marvin and Klein, 1964), numerous zircons have nevertheless been identified and dated from several eucrites, which provide an important constraint on the igneous differentiation on 4 Vesta (Bukovanská et al., 1991, 1996, 1997; Ireland and Bukovanská, 1992, 2003; Ireland and Wlotzka, 1992; Ireland et al., 1992; Bukovanská and Ireland, 1993; Srinivasan et al., 2004; Misawa et al., 2005; Lee et al., 2009). We note, however, with the exception of Ireland and Wlotzka (1992), Ireland and Bukovanská (2003), and Misawa et al. (2005), the rest of the studies remain in the brief abstract form of numerous conference reports. Without exception, U–Pb age dating of zircons in eucrites has relied on the use of secondary ion mass spectrometry (SIMS), such as SHRIMP (Sensitive High Resolution Ion Microprobe) (Ireland and Bukovanská, 1992, 2003; Bukovanská and Ireland, 1993; Misawa et al., 2005; Lee et al., 2009), and Cameca IMS-1270 (Srinivasan et al., 2004) ion microprobes. However, zircons in eucrites are typically small (<5 μm grains are most common), which in the past has limited the application of SIMS technique for U–Pb dating. Both SHRIMP and Cameca IMS 1270 dating of eucrite zircons were limited to a typical grain size of 10–30 μm. For example, Misawa et al. (2005) stated "many of the zircon grains found in basaltic eucrites examined here were too small for SHRIMP analysis (10 μm in size)".

Stern et al. (2005) used a NanoSIMS to perform U–Pb age dating at < 5 μm length scales. However, the technique has two major limitations in recovering the secondary ion signal as the primary beam size is reduced dramatically: (1) Limited by its geometry (smaller magnet and spherical electrostatic sector analyzer radius), NanoSIMS has lower secondary ion sensitivity of $Pb^+$ (3–4 cps/ppm/nA using $O^-$) (Stern et al., 2005), about one third of the large–geometry ion probes with higher transmission, such as SHRIMP, Cameca IMS-1270/1280 (e.g., Liu et al., 2011). (2) NanoSIMS cannot use the "oxygen flooding", a technique of bleeding oxygen gas onto the sample surface known to enhance the secondary $Pb^+$ signal significantly on Cameca IMS-1280 (Schuhmacher et al., 1994; Li et al., 2010). Cameca IMS-1280 uses turbo pump for the sample source, thus oxygen leaked into the source is efficiently pumped away. To ensure high spatial resolution of < 50 nm on a NanoSIMS, turbo pump was not used to avoid vibration. Instead NanoSIMS uses ion getter pump to maintain high vacuum in the sample chamber, which limit the gas load into the system. In addition, in NanoSIMS, the lens stacks are very compact and very close to the sample surface compared to the 1270/1280 system. The co-axial primary focus beam (EOP plate) at negative 8500 V for $O^-$, with a voltage difference at 16,500 V in NanoSIMS (as opposed to 10,000 V for 1270/1280 V) may become the source of arching at elevated pressure more than $10^{-6}$ torr.

Therefore, technical development of U–Pb dating at the scale of < 5 μm on a large geometry instrument with higher sensitivity would offer a better potential to date those tiny zircons found in eucrites and other extraterrestrial materials. Small beam techniques were recently developed for isotope analyses of major elements, such as oxygen using 1 μm $Cs^+$ primary beam (e.g. Page et al., 2007) and magnesium using 3 μm $O^-$ primary beam (Kurahashi et al., 2008). In this paper, we present details of our newly developed small-spot capability for ultra trace Pb isotope analyses using the new generation Cameca IMS-1280 ion microprobe at the 3–4 μm lateral scale, building upon earlier works in our laboratory by Li et al. (2009, 2010) and Liu et al. (2011). We then present our first Pb–Pb and U–Pb age results of 84 analyses of 32 zircon grains obtained from five eucrite samples. These new data were then synthesized with published chronological data on howardites, eucrites and diogenities obtained using both short and long-lived chronometers, to gauge the magmatic history on Vesta during its first 50 Ma. A thermal model is constructed to aid our understanding of Vesta's longevity of magmatism.

## 2. SAMPLE DESCRIPTIONS

The samples studied here are five monomict non-cumulate eucrite. They are all polished thin sections provided by the US National Museum of Natural History (USNM), including Cachari (USNM 3258–1), Béréba (USNM 5745–1), Caldera (USNM 6394–3), Camel Donga (USNM 6429–1) and Juvinas (USNM 439–4). Most of the eucrites here are coarse-grained and granular in texture and composed mainly of plagioclase and pyroxene with minor amount of tridymite, chromite and ilmenite (Figs. 1 and 2). Most of the pyroxenes show exsolution lamellae. The plagioclase is anhedral and calcic. Ilmenite and chromite occur as individual grains. Zircons are associated with ilmenite in most cases with subhedral shapes.

### 2.1. Cachari

Cachari is a monomict breccia of non-cumulate eucrite, found in May, 1916, near Cachari railway station in Azul, Buenos Aires province, Argentina. The total recovered mass is 23.5 kg. Cachari was first described by Ducloux (1921), and subsequently in more detail by Lacroix (1926) and Ducloux (1928). Modern reviews of mineral chemistry, petrogenesis, and evaluation of chemical

Author's personal copy



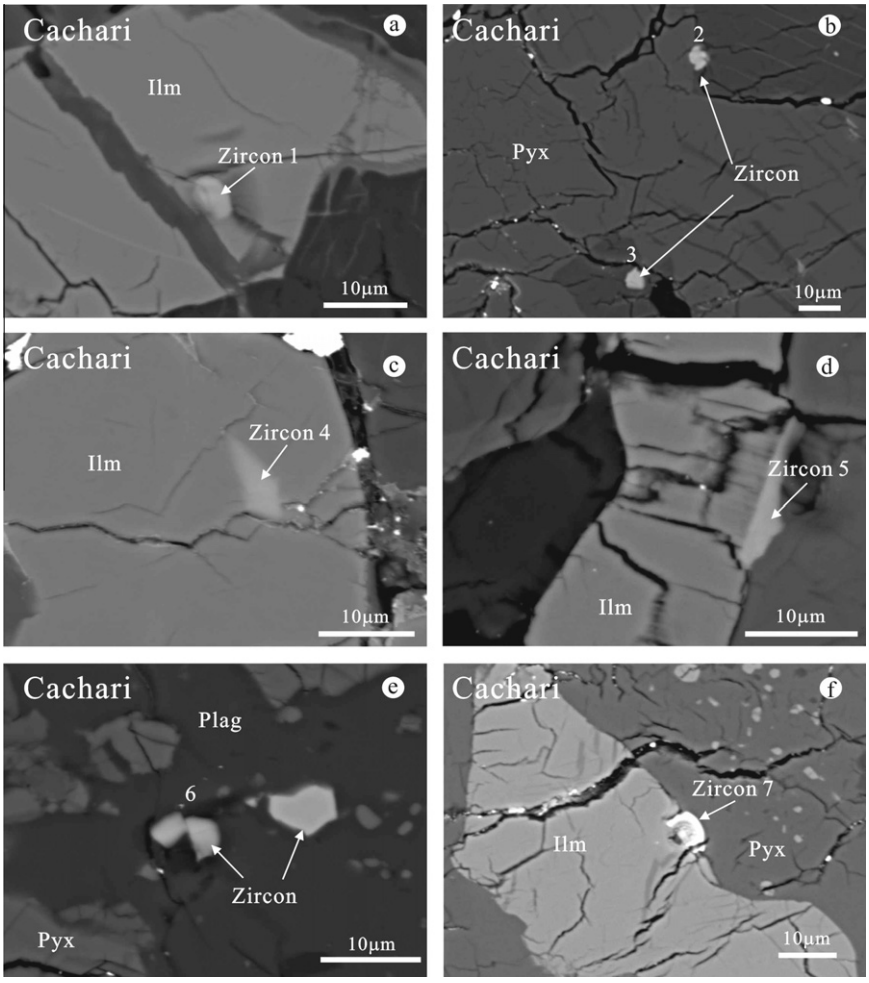


Fig. 1. Backscattered electron (BSE) image of a polished thin section of Cachari eucrite, containing pyroxene (Pyx), plagioclase (Plag), ilmenite (Ilm), chromite (Chrm) and zircon. The zircon grains are associated with ilmenite in (a), (c), (d) and (f), with pyroxene in (b), and with plagioclase in (e). Zircon grain number from 1 to 6 correspond to the Pb/Pb data reported in Table 1. Zircon grain-7 corresponds to the U–Pb data of Cachari shown in Table 2.

composition can be found in Kitts and Lodders (1998). It contains characteristic dark, glassy veins of impact origin (Fredriksson and Kraut, 1967; Boctor et al., 1987). Mafic glass veins or clasts indicate its high degree of shock metamorphism. The bulk chemical compositions of the mafic glass vary within narrow limits and are similar to those of other eucrites (Bogard et al., 1985).

The age of Cachari eucrite has been studied by multiple chronometric methods. Bogard et al. (1985) first dated this meteorite using the Ar–Ar method and obtained ages of $3.04 \pm 0.7$ and $3.47 \pm 0.4$ Ga for the host phase and impact glass veins, respectively. They suggested that the time of glass formation (i.e., time of brecciation) is most likely given by the 3.04 Ga event. The older age of 3.47 Ga for the glass is interpreted as due to greater resistance to Ar diffusion in glass compared to host phases. Interestingly, Pu–Xe dating conducted by Shukolyukov and Begemann (1996a) yielded an age of ~4498 Ma for a bulk sample of Cachari, ~20 Ma younger than that of the glass (~4517 Ma), and they inferred Pu–Xe system of the bulk sample had been reset. Tera et al. (1997) were able to construct a Sm–Nd errorchron with a poorly-constrained age of $3.99 \pm 0.21$ Ga due to limited spread in Sm/Nd ratios. Tera et al. (1997) also report Pb–Pb mineral isochron ages of 4.453 and 4.13 Ga for Cachari. Importantly, they concluded that three non-cumulate eucrites (Stannern, Cachari, and Béréba) showed strong evidence of isotope resetting at about 4 Ga, coinciding with the period of late heavy bombardment in the inner Solar System (also known as "Lunar Cataclysm" for the Moon) (Tera et al., 1974; Gomes et al., 2005; Strom et al., 2005). Additional Ar–Ar, Pb–Pb and Sm–Nd impact resetting ages are discussed in Bogard (1995). Using the zircon U–Pb dating technique, Bukovanská and Ireland (1993) found that the zircon data in Cachari formed a discordia between ~4.2 and 4.56 Ga. Clearly Cachari eucrite underwent a complex thermal history shown by the disturbed Ar–Ar, Pu–Xe, Sm–Nd and Pb–Pb isotopic systems at both whole rock and mineral scales, masking the information for its true crystallization age.

### 2.2. Béréba

Béréba is also a monomict breccia of non-cumulate eucrite, an observed fall in 1924, in Houet, Burkina Faso province, Africa. The total recovered mass is 18 kg. Manhes et al. (1975) first dated with the Rb–Sr method and obtained the internal isochron of 4.3 Ga for Béréba. Subsequently, Birck and Allègre (1978) obtained an internal isochron of $4170 \pm 260$ Ma for Béréba. Both of these isochron ages are significantly lower than 4.55 Ga, indicating the

Author's personal copy



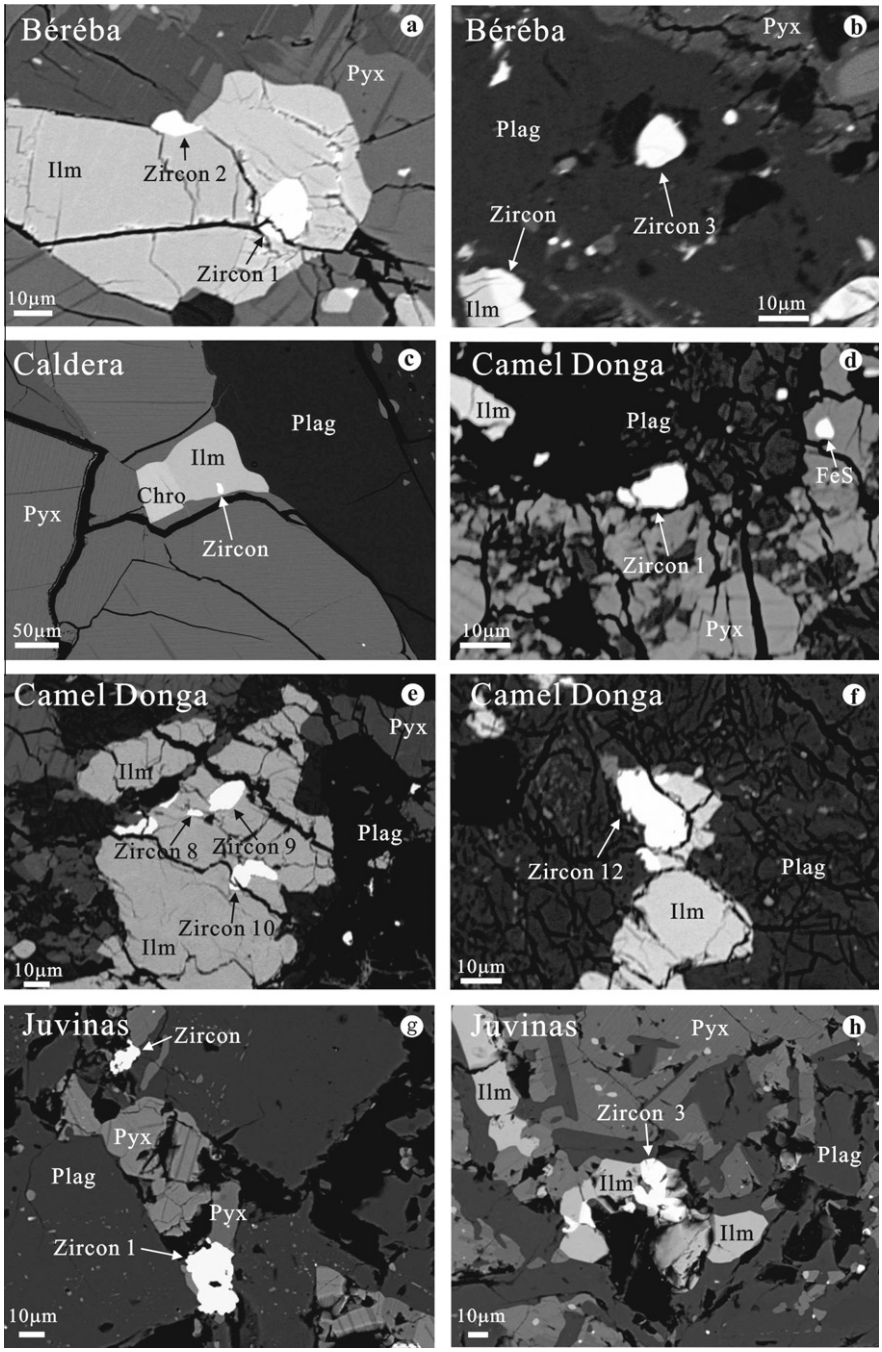


Fig. 2. Backscattered electron (BSE) image of polished thin sections of Béréba, Caldera, Camel Donga and Juvinas eucrites, containing pyroxene (Pyx), plagioclase (Plag), ilmenite (Ilm) and zircon. The zircon grains associated with ilmenite are shown in (a), (c), (e), (f) and (h), with pyroxene in (g), with plagioclase in (b) and (d). Zircon grain number corresponds to the data in Table 2.

disturbance of the Rb–Sr system. Shukolyukov and Begemann reported the K–Ar age of 3310 Ma (Shukolyukov and Begemann, 1996b) and the Pu–Xe age of 4498 ± 16 Ma (Shukolyukov and Begemann, 1996a) for Béréba, assuming the Pb–Pb age of 4557.8 Ma as the absolute crystallization age for Angra dos Reis (ADOR) in their calculation for Pu–Xe age (Lugmair and Galer, 1992). Miura et al. (1998) recalculated the Pu–Xe age for Béréba to be 4512 ± 18 Ma, using the same age anchor of Lugmair and Galer (1992) for ADOR. Pb–Pb mineral isochron age for Béréba had been reported by Carlson et al. (1988) as 4522 ± 4 Ma and Tera et al. (1997) as 4521 ± 4 Ma. With a SHRIMP ion microprobe, Bukovanská and Ireland (1993) first obtained the U–Pb age of 4534 ± 16 Ma for zircons in Béréba. Béréba also displays characteristic dark, glassy veins of impact origin (Carlson et al., 1988), the U–Pb age of ~4.2 Ga was obtained for the phosphate in the dark glassy vein using Cameca IMS-1280 (Zhou et al., 2011). From the above dating results, meteorite of Béréba may have suffered an impact event probably at 4520 Ma, which would not only disturb most of the isotopic systems but also probably result in the presence of mafic glass vein.

Author's personal copy



### 2.3. Caldera

Caldera is a monomict unbrecciated non-cumulate eucrite, found in 1967, in Caldera, Atacama, Chile. The total recovered mass is 500 g. Caldera is the only unbrecciated non-cumulate eucrite in our set of samples. Texturally, it is different from the other brecciated noncumulate eucrites in having a relatively coarse grain size (typically a few millimeters) (Fig. 2c) and hypidiomorphic granular texture. Pu–Xe age of ~4513 Ma has been reported by Shukolyukov and Begemann (1996a), assuming 4557.8 Ma as the absolute crystallization age for ADOR (Lugmair and Galer, 1992). Combining the long-lived $^{147}Sm$–$^{143}Nd$ age (4544 ± 19 Ma) and the short-lived $^{146}Sm$–$^{142}Nd$ and $^{53}Mn$–$^{53}Cr$ data, Wadhwa and Lugmair (1996) obtained a high resolution age of 4537 ± 12 Ma as the crystallization age for Caldera. The Pb–Pb isotope data of plagioclase and pyroxene in Caldera defined an age of 4516.1 ± 2.8 Ma (Galer and Lugmair, 1996). Since the unbrecciated and large grain size for Caldera implied cooling rates after recrystallization was very slow, it appears plausible that these ages discrepancy reflect different temperatures for isotopic closure system.

### 2.4. Camel Donga

Camel Donga is a monomict breccia of non-cumulate eucrite, found in January 1984, on the Nullarbor Planin, Western Australia. The total weight is 25 kg. Compared to the other eucrites, Camel Donga was strongly shocked and characterized by the high content of metallic iron in mineralogy (about 2%, Palme et al., 1988). The age of Camel Donga eucrite was limited in literatures. Pu–Xe age of 4521 ± 20 Ma was reported by Shukolyukov and Begemann (1996a), and 4507 ± 16 Ma by Miura et al. (1998), anchored to the Pb–Pb age of 4557.8 Ma for ADOR (Lugmair and Galer, 1992). The large number of zircons present in the thin section provides the opportunity to improve the limited geochronological information for Camel Donga.

### 2.5. Juvinas

Juvinas is a monomict breccia of a non-cumulate eucrite, also an observed fall in 1821, in Rhone-Alpes, France. The total recovered mass is 91 kg. Lugmair (1974) dated Juvinas with the Sm–Nd method and obtained the internal isochron of 4560 ± 80 Ma. Shukolyukov and Begemann (1996a) reported the Pu–Xe age of 4551 ± 15 Ma, assuming 4557.8 Ma as the Pb–Pb age for ADOR (Lugmair and Galer, 1992). Miura et al. (1998) also reported the Pu–Xe age for Juvinas to be 4548 ± 23 Ma, using the same age anchor of Lugmair and Galer (1992) for ADOR. However, isotopic systematics of Ar–Ar and Pb–Pb internal isochron indicated thermal event at around 4–4.1 Ga (Kaneoka et al., 1995) and 4320.7 ± 1.7 Ma (Galer and Lugmair, 1996) for Juvinas respectively. With a SHRIMP ion microprobe, Bukovanská and Ireland (1993) first obtained the U–Pb age of ~4560 Ma for zircons and later Lee et al. (2009) obtained 4527 ± 24 Ma.

## 3. ANALYTICAL TECHNIQUES

Prior to in situ Pb–Pb and U–Pb analyses, the thin sections of eucrite samples were imaged with reflected light microscope and LEO 1450VP scanning electron microscope (SEM) equipped with a Inca Energy 300 energy dispersive (ESD) X-ray analysis system to select suitable analytical spots, i.e. to avoid micro fractures, inclusions and other noted physical defects in the individual zircon grains.

The Cachari thin section was Au-coated prior to SIMS analyses for Pb–Pb dating in multicollection mode. All other sections were C-coated instead prior to U–Pb analyses in mono-collection mode. In-situ isotopic analysis of Pb–Pb and U–Pb were performed on a large radius magnetic sector multi-collector Cameca IMS-1280 ion microprobe at the Institute of Geology and Geophysics, Chinese Academy of Sciences in Beijing.

### 3.1. The small beam technique with the Gaussian illumination probe

We exploit a number of technical development and features on the new Cameca IMS-1280 ion microprobe to achieve precise Pb–Pb and U–Pb dating on zircons of < 5 μm.

First, in conventional SIMS U–Pb isotope measurements with a typical lateral resolution of 10–30 μm, the primary oxygen ion beam is tuned in so-called Köhler mode, with homogeneous density distribution generating flat sputtered craters on the sample target. Beam size in Köhler mode is completely defined by the apertures. Cameca IMS-1280 ion probe offers a second alternative mode of primary ion beam. In the so-called Gaussian mode, the primary ions have intensity distribution like Gaussian distribution, yet with edges cut (by the last primary aperture) to reduce aberration and define a precise beam size and shape with higher density at the center. In this study, we use finely focused, continuously variable primary $O_2^-$ beam in Gaussian mode to sputter zircons < 5 μm generating a fat "U" shape bottom, to maximize intensity at the center. The pros and cons on the choice of $O_2^-$ or $O^-$ as the primary ion beam species were discussed in Liu et al. (2011).

Second, the primary beam intensity of oxygen is tuned to only 0.1–0.2 nA, as opposed to a typical 8–15 nA used in Köhler mode for larger spot. This is two orders of magnitude lower than the routine analysis. This primary ion beam of $O_2^-$ was accelerated at −13 kV.

Third, an "oxygen flooding technique", i.e. the introduction of oxygen into sample chamber, was used with a working $O_2$ gas pressure of $\sim 1 \times 10^{-5}$ torr to enhance the secondary $Pb^+$ ion yield (*c.f.* Schuhmacher et al., 1994; Li et al., 2010). Without $O_2$ flooding, the secondary $Pb^+$ sensitivities for zircons is about 12–13 cps/ppm/nA at resolving power of 8000. With oxygen flooding, $Pb^+$ sensitivities are increased by a factor of 2 for zircons (Fig. 3) (Li et al., 2010). This is crucial to improve the precision of $^{207}Pb/^{206}Pb$ measurement.

Fourth, smaller primary beam size permits us to use higher magnification transfer settings of ~260 for secondary ions of $Pb^+$ to ensure higher transmission (~21 cps/ppm/nA using $O_2^-$) and improve precision (Liu et al., 2011). Positive secondary ions were extracted with a 10 kV potential.

The size and quality of the finely tuned primary beam of $O_2^-$ were checked and assessed by scanning across a standard target material, where Ta grid (evenly distributed between 1 and 5 μm) laid on top of Si substrate (Fig. 4), and by detecting $^{28}Si^+$ signal from the substrate. If the pri-

Author's personal copy



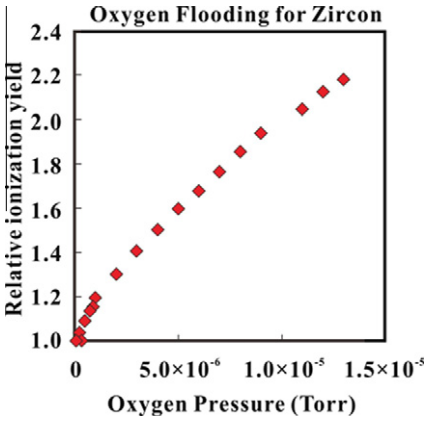


Fig. 3. With oxygen flooding technique used in this study, the secondary $Pb^+$ sensitivities are increased by a factor of 2 for zircons.

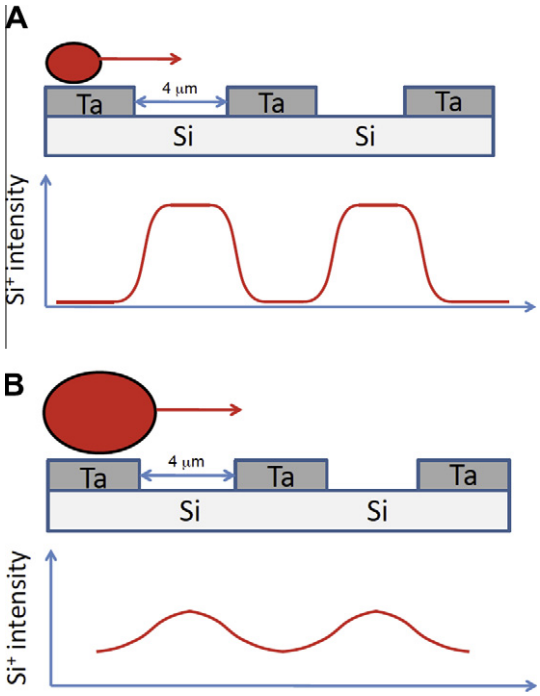


Fig. 4. Method to check the quality and sizes of the primary beams of $O_2^-$. By scanning the primary beams across the Ta grid (predefined with even spacing between 1 and 5 μm) laid on top of Si substrate, and observing the peak shape of $^{28}Si^+$ signal, acceptable (A) and unacceptable (B) tuning status were established.

mary beam size is properly tuned to the desired size (defined by the Ta grid spacing), a flat peak top is expected and was observed (Fig. 4A). If the primary beam size was larger than the desired, a fat point peak of $^{28}Si^+$ signal was observed instead (Fig. 4B). The quality of the primary beam was further checked and confirmed on the analyzed eucrite zircons (Béréba) by using Atomic Force Microscopy (AFM) shown in Fig. 5.

Prior to data collection, the target sampling area was typically rastered with the primary beam of ~2 nA for 2 min to expose the fresh surface area and remove common Pb contamination (Fig. 5A). The secondary ion image of $^{90}Zr_2{}^{16}O^+$ signal (Fig. 5B) from rastering helps to precisely define the target area to aim the finely tuned primary beam of $O_2^-$. Since the zircons in eucrites in this study are mostly ~5 μm or less, we could not perform multiple spot analyses on the individual grains without overlapping. In order to maximize useful data generation on small zircon grains, multiple, overlapping analyses were made by moving the primary beam 1–2 μm apart after each analysis. For Pb isotopes analyses, each measurement consists of 80 cycles, and the total analytical time is ca. 15 min. The depth of the sputtered zircon was typically ~400 nm (Fig. 5F and G) after single analyses. After three repeated measurements by moving primary beam at a step of 1–2 μm apart, the crater holes were ~1.5 μm (Fig. 5D and E).

### 3.2. Multicollector mode for Pb–Pb age dating

In the secondary ion beam optics, a 60 eV energy window was used to reduce the tailing effect. A mass resolving power of ca. 8000 (at 50% peak height) was sufficient for separation of $Pb^+$ peaks from isobaric interferences (Fig. 6). The entrance and exit slits were set to 52 and 151 μm, respectively. Under these conditions, the sensitivity for $Pb^+$ was ~21 cps/ppm/nA using $O_2^-$ (Liu et al., 2011) calculated against the M257 standard zircon (Nasdala et al., 2008).

Secondary ion beams of $^{204}Pb$, $^{206}Pb$, $^{207}Pb$ and $^{90}Zr_2{}^{16}O_2$ were measured simultaneously in static multi-collector mode with four ion-counting electron multipliers (EMs). In addition, the NMR (Nuclear Magnetic Resonance) controller was used in multi-collector measurements to stabilize the magnetic field, resulting in an instrumental drift ($\Delta M/M$) less than 2.5 ppm over 16 h (Li et al., 2009). The $^{90}Zr_2{}^{16}O_2{}^+$ signal was used as reference peak for tuning the secondary ions. Difference between the measured $^{207}Pb/^{206}Pb$ ratios of the Phalaborwa baddeleyite and its recommended value of 0.127198 was applied to calibrate the secondary ion yields for each EMs on the movable trolleys relative to the axial one.

Factors that may affect the Pb isotope measurement, including instrumental mass fractionation of Pb isotopes, Pb hydrides and drift of EMs' efficiencies, were monitored by analyses of Phalaborwa baddeleyite standard, since the matrix effect on mass fractionation of $^{207}Pb/^{206}Pb$ is known to be negligible between zircon and baddeleyite (Ireland and Williams, 2003). Difference between the measured $^{207}Pb/^{206}Pb$ ratios of the Phalaborwa baddeleyite and its recommended value of 0.127198 ($t_{207/206} = 2059.6$ Ma, Heaman, 2009) was applied to an external correction of $^{207}Pb/^{206}Pb$ ratios of unknowns. A daily variation of the measured $^{207}Pb/^{206}Pb$ ratios of the Phalaborwa baddeleyite is usually within 0.2%. Correction of common Pb was made by measuring the amount of $^{204}Pb$, and assuming the Canyon Diablo troilite (CDT) Pb isotopic compositions ($^{206}Pb/^{204}Pb = 9.307$, $^{207}Pb/^{206}Pb = 1.09861$, Tatsumoto

Author's personal copy



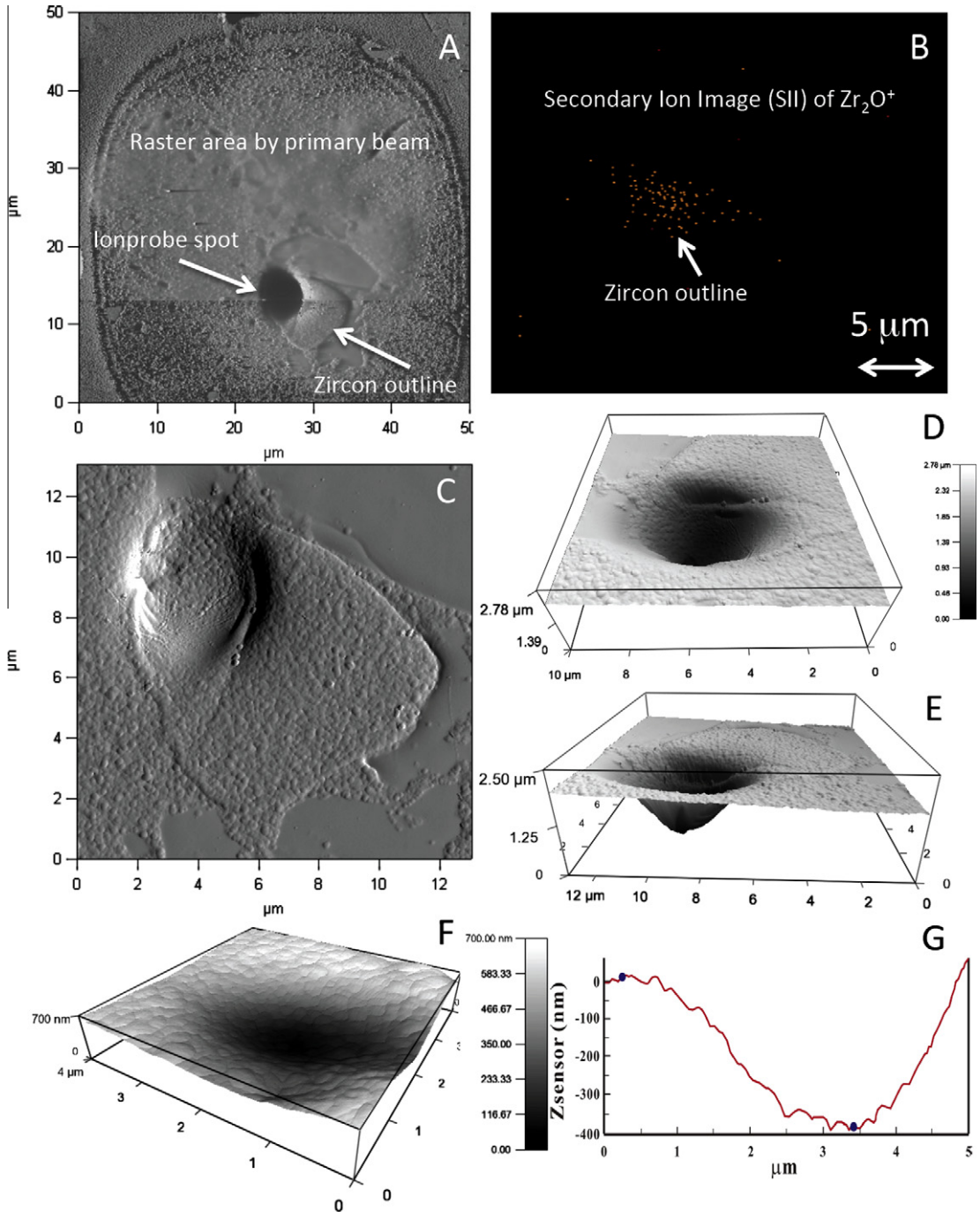


Fig. 5. (A) Atomic Force Microscopy (AFM) image of target area that was rastered with the primary $O_2^-$ beams to clean the surface and remove common Pb contamination. (B) The secondary ion image of $^{90}Zr_2{}^{16}O^+$ from rastering step (5A) was used to precisely define the area of interest to place the finely tuned primary beam. Sputtered ion probe spots after U–Pb analyses were characterized with AFM (C–G). All zircons are from Béréba. C (shown in 2D) and D, and E (shown in 3D) are AFM images of one zircon on which analyses were repeated three times by moving primary beam 1–2 μm across after each analysis. F and G show the depth profile in 3D and 2D for two other zircons from Béréba, where only single analysis was performed. Note that D–G is not to scale in vertical and horizontal axis, e.g., vertical scale is exaggerated by ~5 times in G. Vertical dimensions shown in D–G illustrate the depth of penetration after analyses, varying between 400 nm (for single analyses) and 1.5 μm (for three repeat analyses), in our typical running conditions specified in the text.

Author's personal copy



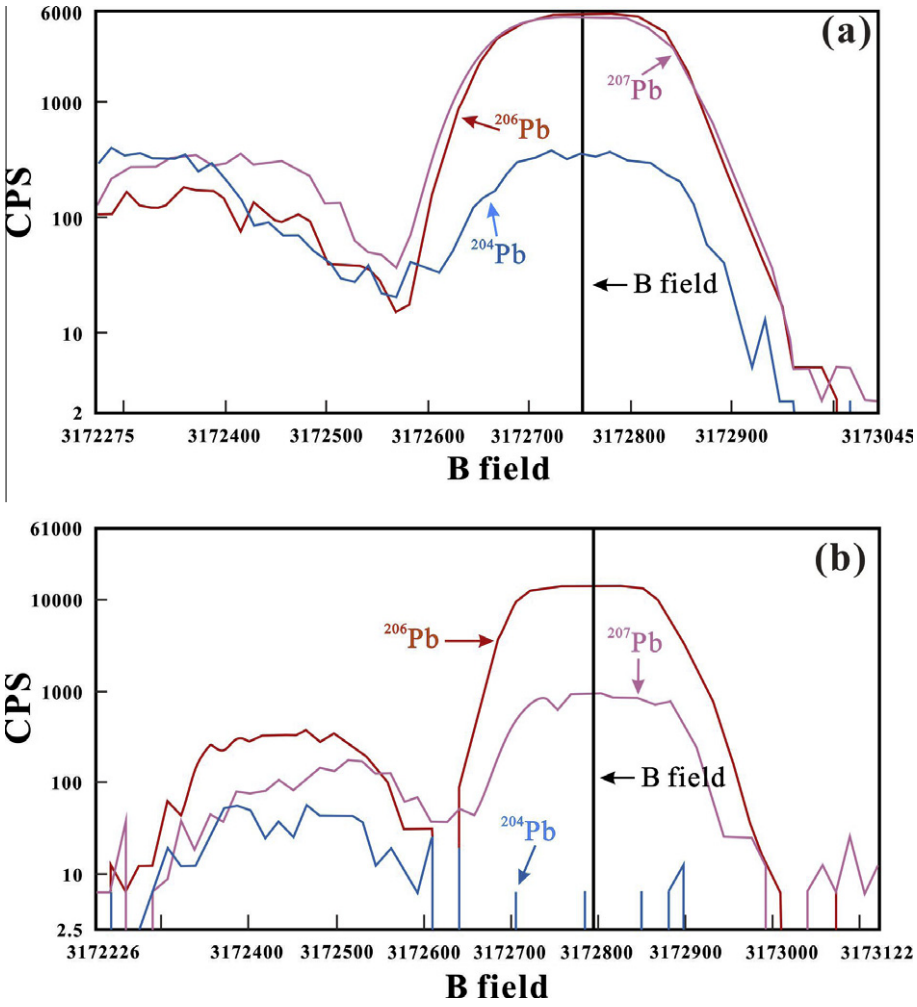


Fig. 6. Mass scan of Pb isotopes with Cameca IMS-1280 multicollector array at a mass resolution of 8000 (defined at 50% peak height), with more than one third of the peak width being flat at the 99% level. *Y* axis is the accumulation of counts per second (CPS) for every isotope; *X* axis (B field) is the magnet current DAC (digital to analog conversion) value which is related to the magnetic flux density. (a) Mass scan of Pb isotopes with NIST 610 to identify the peak of $^{204}$Pb. (b) Mass scan of zircon M257 zircon standard. Every single scan could obtain 150–160 cps for $^{206}$Pb.

et al., 1973). Uncertainties for individual analyses in Table 1 are reported as 1$\sigma$. Weighted average ages for pooled Pb/Pb analyses are quoted with 95% confidence interval (2$\sigma$) with the Isoplot programs of Ludwig (2003).

### 3.3. Monocollector for U–Pb dating

We have also conducted U–Pb dating with a small beam of $< 5$ μm under single-collector mode. Technical details for mono detection mode for U–Pb dating can be found in Liu et al. (2011) and are described here only briefly. $^{180}Hf^{16}O$ peak is used as reference for peak centering. $^{92}Zr_2{}^{16}O$, $^{204}$Pb, $^{206}$Pb, $^{207}$Pb, $^{208}$Pb, $^{238}$U and $^{238}U^{16}O_2$ were measured on axial electron multiplier in peak jumping mode. The ellipsoidal spot is about $3 \times 4$ μm in size (Fig. 5). Mass resolving power is set at 7000 (50% peak height definition) with entrance slit 55 μm and 173 μm exit slit. Each measurement for U–Pb dating consists of 15 cycles, taking nearly 15 min. Pb/U fractionation was calibrated according to the power relationship between $^{206}Pb/^{238}U$ and $^{238}U^{16}O_2/^{238}U$. Zircon standard M257 ($^{206}Pb/^{238}U = 0.09100 \pm 0.00003$; $^{207}Pb/^{235}U = 0.7392 \pm 0.0003$; $t_{206/238} = 561.3 \pm 0.3$ Ma, Nasdala et al., 2008) is used as a standard to calibrate Pb/U fractionation and U content. The age would be determined with precision and accuracy of 1–2% using a spot less than 5 μm. Correction of common Pb was made by measuring the amount of $^{204}$Pb and the CDT Pb isotopic compositions (Tatsumoto et al., 1973). The results are listed in Table 2 and uncertainties for individual analyses are reported as 1$\sigma$. Weighted average ages for pooled Pb/Pb analyses are quoted with 95% confidence interval (2$\sigma$) using the Isoplot programs of Ludwig (2003).

## 4. ANALYTICAL RESULTS

### 4.1. Multicollection Pb–Pb dating results for Cachari

In situ $^{207}Pb^*/^{206}Pb^*$ isotope ratios measured in six zircon grains in Cachari are provided in Table 1 and their

Author's personal copy





Table 1
SIMS Pb–Pb isotopic data of the Cachari zircon.

| Sample spot ID | $^{90}Zr_2{}^{16}O_2$ (cps) | U[a] ppm | $^{207}Pb$ (cps) | $^{204}Pb/^{206}Pb_m$ | $\pm1\sigma$ (%) | $^{207}Pb/^{206}Pb_m$ | $\pm1\sigma$ | $^{207}Pb/^{206}Pb_{c1}$ | $\pm1\sigma$ | $T_{207/206\ (c1)}$ (Ma) | $\pm1\sigma$ | $^{207}Pb/^{206}Pb_{c2}$ | $\pm1\sigma$ | $T_{207/206\ (c2)}$ (Ma) | $\pm1\sigma$ |
|---|---|---|---|---|---|---|---|---|---|---|---|---|---|---|---|
| Cachari@1–1 | 306 | 23 | 69 | 0.00045 | 16 | 0.6164 | 0.61 | 0.6128 | 1.2 | 4539 | 17 | 0.6130 | 1.2 | 4539 | 18 |
| Cachari@1–2 | 262 | 20 | 61 | 0.00026 | 25 | 0.6132 | 0.65 | 0.6105 | 1.2 | 4533 | 17 | 0.6106 | 1.2 | 4533 | 18 |
| Cachari@1–3 | 168 | 41 | 47 | 0.00093 | 12 | 0.6513 | 0.62 | 0.6203 | 1.1 | 4556 | 17 | 0.6207 | 1.1 | 4557 | 16 |
| Cachari@2–1 | 202 | 25 | 28 | 0.00063 | 19 | 0.6408 | 0.80 | 0.6114 | 1.3 | 4535 | 19 | 0.6116 | 1.3 | 4536 | 19 |
| Cachar@3–1 | 1151 | 49 | 156 | 0.00043 | 12 | 0.6336 | 0.41 | 0.6301 | 1.1 | 4579 | 16 | 0.6303 | 1.1 | 4580 | 16 |
| Cachar@3–2 | 1225 | 51 | 163 | 0.00021 | 16 | 0.6363 | 0.41 | 0.6338 | 1.1 | 4587 | 16 | 0.6339 | 1.1 | 4588 | 16 |
| Cachar@3–3 | 1281 | 54 | 171 | 0.00015 | 19 | 0.6397 | 0.39 | 0.6374 | 1.1 | 4596 | 16 | 0.6375 | 1.1 | 4596 | 16 |
| Cachar@4–1 | 193 | 27 | 28 | 0.00089 | 16 | 0.6551 | 0.80 | 0.6242 | 1.3 | 4565 | 19 | 0.6246 | 1.3 | 4566 | 19 |
| Cachar@4–2 | 132 | 20 | 20 | 0.00101 | 18 | 0.6470 | 0.94 | 0.6158 | 1.4 | 4546 | 21 | 0.6162 | 1.4 | 4547 | 21 |
| Cachar@5–1 | 254 | 11 | 32 | 0.00003 | 100 | 0.6026 | 0.91 | 0.6009 | 1.3 | 4510 | 19 | 0.6009 | 1.3 | 4510 | 19 |
| Cachar@5–2 | 300 | 11 | 32 | $<10^{-6}$ | 100 | 0.6050 | 0.90 | 0.6035 | 1.3 | 4516 | 19 | 0.6035 | 1.3 | 4516 | 19 |
| Cachar@5–3 | 549 | 27 | 72 | 0.00027 | 26 | 0.6343 | 0.68 | 0.6066 | 1.2 | 4524 | 18 | 0.6067 | 1.2 | 4524 | 18 |
| Cachar@5–4 | 461 | 25 | 67 | 0.00033 | 23 | 0.6517 | 0.71 | 0.6231 | 1.2 | 4563 | 18 | 0.6233 | 1.2 | 4563 | 18 |
| Cachar@5–5 | 405 | 20 | 51 | 0.00031 | 28 | 0.6413 | 0.81 | 0.6132 | 1.3 | 4540 | 19 | 0.6133 | 1.3 | 4540 | 19 |
| Cachar@6–1 | 185 | 29 | 29 | 0.00065 | 18 | 0.6511 | 0.78 | 0.6212 | 1.3 | 4558 | 19 | 0.6215 | 1.3 | 4559 | 19 |
| Cachar@6–2 | 197 | 28 | 30 | $<10^{-6}$ | 100 | 0.6294 | 0.77 | 0.6031 | 1.2 | 4515 | 19 | 0.6031 | 1.2 | 4515 | 17 |
| Cachar@6–3 | 147 | 24 | 26 | 0.00126 | 14 | 0.6560 | 0.84 | 0.6235 | 1.3 | 4564 | 20 | 0.6241 | 1.3 | 4565 | 20 |

m: Measured values; c1: corrected values using CDT Pb as common lead composition ($^{206}Pb/^{204}Pb = 9.307$, $^{207}Pb/^{206}Pb = 1.09861$, Tatsumoto et al., 1973); c2: corrected values using terrestrial Pb as common lead composition ($^{206}Pb/^{204}Pb = 18.7$, $^{207}Pb/^{206}Pb = 0.84$, Stacey and Kramers, 1975). Error of corrected $^{207}Pb/^{206}Pb$ includes error of measured $^{207}Pb/^{206}Pb$, common Pb correction and Phalaborwa standard propagation.

[a] U concentration in this table is estimated by assuming U–Pb concordancy.

Author's personal copy





Table 2
SIMS U–Pb isotopic data of zircon from non-cumulate eucrite.

| Sample | Spot | $^{92}Zr_2{}^{16}O$ (cps) | U (ppm) | Th (ppm) | Th/U | $^{207}Pb^*/^{206}Pb^*$ | ±1σ (%) | $^{207}Pb^*/^{235}U$ | ±1σ (%) | $^{206}Pb^*/^{238}U$ | ±1σ (%) | $t_{207/206}$ (Ma) | ±1σ | $t_{207/235}$ (Ma) | ±1σ | $t_{206/238}$ (Ma) | ±1σ |
|---|---|---|---|---|---|---|---|---|---|---|---|---|---|---|---|---|---|
| Cachari | 7–1 | 278 | 105 | 22 | 0.21 | 0.6087 | 0.88 | 87.3 | 3.2 | 1.040 | 2.79 | 4529 | 13 | 4549 | 32 | 4596 | 93 |
| | 7–2 | 223 | 147 | 32 | 0.22 | 0.6224 | 0.92 | 88.4 | 2.9 | 1.030 | 2.48 | 4561 | 13 | 4562 | 29 | 4565 | 81 |
| | 7–3 | 183 | 197 | 46 | 0.23 | 0.6196 | 0.69 | 90.6 | 2.7 | 1.060 | 2.42 | 4555 | 10 | 4586 | 27 | 4659 | 81 |
| Béréba | 1–1 | 288 | 48 | 11 | 0.22 | 0.6029 | 1.73 | 77.1 | 3.3 | 0.927 | 2.86 | 4515 | 25 | 4425 | 34 | 4229 | 89 |
| | 1–2 | 319 | 57 | 12 | 0.21 | 0.6256 | 1.41 | 89.3 | 2.9 | 1.035 | 2.57 | 4569 | 20 | 4572 | 30 | 4579 | 85 |
| | 2 | 307 | 46 | 19 | 0.42 | 0.6272 | 1.78 | 88.5 | 3.1 | 1.022 | 2.56 | 4574 | 26 | 4563 | 32 | 4539 | 84 |
| | 3–1 | 426 | 48 | 112 | 2.34 | 0.6170 | 1.33 | 95.2 | 3.6 | 1.119 | 3.33 | 4549 | 19 | 4637 | 37 | 4841 | 114 |
| | 3–2 | 299 | 50 | 72 | 1.44 | 0.6154 | 1.65 | 82.3 | 3.1 | 0.969 | 2.61 | 4545 | 24 | 4490 | 31 | 4369 | 83 |
| Caldera | 1–1 | 139 | 13 | 28 | 2.10 | 0.6354 | 2.40 | 89.6 | 6.6 | 1.022 | 6.17 | 4591 | 34 | 4575 | 69 | 4540 | 204 |
| | 1–2 | 156 | 8 | 20 | 2.43 | 0.5975 | 3.16 | 82.3 | 7.1 | 1.000 | 6.33 | 4502 | 45 | 4491 | 74 | 4467 | 207 |
| | 1–3 | 152 | 16 | 25 | 1.55 | 0.5925 | 2.06 | 99.4 | 4.8 | 1.216 | 4.35 | 4490 | 30 | 4680 | 50 | 5131 | 156 |
| | 1–4 | 138 | 16 | 28 | 1.72 | 0.6276 | 2.01 | 102.8 | 4.3 | 1.188 | 3.76 | 4573 | 29 | 4714 | 44 | 5048 | 133 |
| Camel Donga | 1–1 | 100 | 146 | 167 | 1.15 | 0.6071 | 0.97 | 79.9 | 3.3 | 0.955 | 3.18 | 4525 | 14 | 4461 | 34 | 4320 | 101 |
| | 1–2 | 114 | 218 | 323 | 1.48 | 0.6302 | 0.84 | 76.7 | 3.2 | 0.882 | 3.14 | 4579 | 12 | 4419 | 33 | 4077 | 96 |
| | 2–1 | 66 | 118 | 51 | 0.43 | 0.6180 | 1.59 | 80.3 | 4.1 | 0.942 | 3.79 | 4551 | 23 | 4466 | 42 | 4279 | 120 |
| | 2–2 | 58 | 167 | 85 | 0.51 | 0.6164 | 1.16 | 84.2 | 3.4 | 0.990 | 3.20 | 4547 | 17 | 4513 | 35 | 4438 | 104 |
| | 3 | 14 | 114 | 215 | 1.89 | 0.6184 | 3.56 | 88.3 | 6.2 | 1.035 | 5.02 | 4552 | 51 | 4561 | 64 | 4582 | 167 |
| | 4 | 67 | 120 | 25 | 0.21 | 0.6018 | 1.36 | 75.6 | 3.5 | 0.911 | 3.25 | 4512 | 20 | 4405 | 36 | 4174 | 101 |
| | 5–1 | 61 | 75 | 25 | 0.34 | 0.6271 | 2.34 | 85.7 | 4.2 | 0.991 | 3.46 | 4572 | 33 | 4531 | 43 | 4439 | 112 |
| | 5–2 | 40 | 77 | 29 | 0.38 | 0.6035 | 2.22 | 81.5 | 4.1 | 0.979 | 3.45 | 4516 | 32 | 4480 | 42 | 4400 | 111 |
| | 5–3 | 74 | 106 | 29 | 0.27 | 0.6097 | 1.38 | 82.5 | 3.5 | 0.982 | 3.24 | 4531 | 20 | 4493 | 36 | 4410 | 104 |
| | 6 | 70 | 66 | 13 | 0.19 | 0.5881 | 2.37 | 100.5 | 4.1 | 1.239 | 3.30 | 4479 | 34 | 4691 | 42 | 5196 | 119 |
| | 7–1 | 98 | 198 | 316 | 1.59 | 0.6160 | 0.99 | 80.6 | 3.4 | 0.949 | 3.20 | 4546 | 14 | 4469 | 34 | 4301 | 101 |
| | 7–2 | 80 | 130 | 180 | 1.39 | 0.6039 | 1.40 | 82.0 | 3.4 | 0.984 | 3.10 | 4517 | 20 | 4486 | 35 | 4417 | 100 |
| | 7–3 | 84 | 214 | 267 | 1.25 | 0.6205 | 0.89 | 77.7 | 3.3 | 0.908 | 3.22 | 4557 | 13 | 4433 | 34 | 4165 | 100 |
| | 7–4 | 84 | 144 | 198 | 1.38 | 0.6090 | 1.44 | 84.2 | 3.4 | 1.002 | 3.10 | 4530 | 21 | 4513 | 35 | 4476 | 101 |
| | 8 | 73 | 96 | 202 | 2.11 | 0.5903 | 1.52 | 91.5 | 3.6 | 1.124 | 3.26 | 4484 | 22 | 4597 | 37 | 4857 | 112 |
| | 9–1 | 85 | 123 | 441 | 3.57 | 0.6160 | 1.31 | 85.6 | 3.5 | 1.008 | 3.21 | 4546 | 19 | 4530 | 35 | 4495 | 105 |
| | 9–2 | 60 | 106 | 264 | 2.48 | 0.6144 | 1.58 | 97.1 | 3.6 | 1.146 | 3.27 | 4542 | 23 | 4657 | 37 | 4923 | 114 |
| | 9–3 | 92 | 99 | 160 | 1.62 | 0.6115 | 1.23 | 79.1 | 3.5 | 0.938 | 3.23 | 4536 | 18 | 4451 | 35 | 4267 | 101 |
| | 9–4 | 38 | 78 | 79 | 1.01 | 0.5849 | 2.08 | 90.6 | 3.8 | 1.123 | 3.13 | 4471 | 30 | 4586 | 38 | 4852 | 108 |

Author's personal copy



| | | | | | | | | | | | | | | | | | |
|---|---|---|---|---|---|---|---|---|---|---|---|---|---|---|---|---|---|
| | 9–5 | 25 | 197 | 342 | 1.73 | 0.5994 | 2.26 | 73.3 | 4.0 | 0.886 | 3.35 | 4507 | 32 | 4374 | 41 | 4091 | 102 |
| | 9–6 | 79 | 56 | 60 | 1.08 | 0.6026 | 1.70 | 86.9 | 3.8 | 1.046 | 3.37 | 4514 | 25 | 4545 | 39 | 4616 | 112 |
| | 9–7 | 44 | 66 | 88 | 1.34 | 0.6112 | 2.58 | 82.9 | 4.4 | 0.984 | 3.58 | 4535 | 37 | 4498 | 45 | 4415 | 115 |
| | 10–1 | 101 | 118 | 398 | 3.38 | 0.6045 | 1.50 | 86.4 | 3.5 | 1.036 | 3.19 | 4519 | 22 | 4539 | 36 | 4584 | 105 |
| | 10–2 | 113 | 62 | 58 | 0.94 | 0.5889 | 1.54 | 79.1 | 3.5 | 0.974 | 3.12 | 4481 | 22 | 4451 | 35 | 4385 | 100 |
| | 10–3 | 82 | 120 | 406 | 3.39 | 0.6071 | 1.30 | 82.8 | 3.4 | 0.990 | 3.18 | 4525 | 19 | 4497 | 35 | 4435 | 103 |
| | 11 | 27 | 67 | 28 | 0.42 | 0.6106 | 3.25 | 84.7 | 4.9 | 1.006 | 3.62 | 4534 | 46 | 4520 | 50 | 4489 | 118 |
| | 12–1 | 86 | 94 | 5 | 0.05 | 0.6243 | 1.30 | 80.9 | 3.4 | 0.940 | 3.14 | 4566 | 19 | 4473 | 35 | 4271 | 99 |
| | 12–2 | 79 | 117 | 15 | 0.13 | 0.6121 | 1.19 | 81.1 | 3.4 | 0.961 | 3.23 | 4537 | 17 | 4476 | 35 | 4343 | 103 |
| | 12–3 | 66 | 130 | 22 | 0.17 | 0.6116 | 1.28 | 77.6 | 3.5 | 0.920 | 3.23 | 4536 | 18 | 4431 | 35 | 4206 | 101 |
| | 12–4 | 84 | 140 | 20 | 0.14 | 0.6260 | 1.07 | 82.8 | 3.4 | 0.959 | 3.23 | 4570 | 15 | 4496 | 35 | 4334 | 103 |
| | 12–5 | 56 | 93 | 12 | 0.13 | 0.6181 | 1.80 | 88.9 | 3.8 | 1.044 | 3.31 | 4551 | 26 | 4568 | 39 | 4607 | 110 |
| | 13 | 57 | 142 | 32 | 0.22 | 0.6012 | 1.51 | 85.0 | 3.6 | 1.025 | 3.23 | 4511 | 22 | 4523 | 36 | 4549 | 106 |
| | 14–1 | 62 | 265 | 58 | 0.22 | 0.5879 | 0.92 | 78.0 | 3.3 | 0.962 | 3.13 | 4478 | 13 | 4437 | 33 | 4346 | 100 |
| | 14–2 | 79 | 145 | 22 | 0.15 | 0.5882 | 1.10 | 75.6 | 3.4 | 0.932 | 3.20 | 4479 | 16 | 4405 | 34 | 4246 | 100 |
| | 14–3 | 67 | 223 | 52 | 0.23 | 0.6050 | 0.96 | 78.8 | 3.3 | 0.945 | 3.17 | 4520 | 14 | 4447 | 34 | 4288 | 100 |
| Juvinas | 1–1 | 98 | 50 | 24 | 0.48 | 0.6133 | 1.70 | 90.1 | 3.6 | 1.065 | 3.13 | 4540 | 24 | 4581 | 36 | 4674 | 105 |
| | 1–2- | 89 | 50 | 22 | 0.44 | 0.5940 | 1.50 | 83.8 | 4.2 | 1.023 | 3.95 | 4493 | 22 | 4508 | 43 | 4541 | 130 |
| | 1–3 | 83 | 53 | 31 | 0.57 | 0.5973 | 1.65 | 87.0 | 3.8 | 1.056 | 3.37 | 4502 | 24 | 4546 | 38 | 4645 | 113 |
| | 1–4 | 70 | 46 | 20 | 0.43 | 0.6135 | 1.68 | 96.8 | 4.2 | 1.145 | 3.87 | 4540 | 24 | 4654 | 43 | 4918 | 134 |
| | 1–5 | 70 | 63 | 26 | 0.41 | 0.6254 | 1.75 | 93.0 | 5.1 | 1.078 | 4.75 | 4568 | 25 | 4613 | 52 | 4715 | 161 |
| | 1–6 | 46 | 86 | 44 | 0.51 | 0.6051 | 1.70 | 99.7 | 3.9 | 1.195 | 3.49 | 4520 | 24 | 4683 | 40 | 5067 | 124 |
| | 1–7 | 57 | 72 | 39 | 0.54 | 0.6153 | 1.65 | 101.7 | 4.7 | 1.199 | 4.36 | 4545 | 24 | 4703 | 48 | 5079 | 155 |
| | 2–1 | 59 | 58 | 18 | 0.31 | 0.6205 | 1.71 | 90.4 | 4.8 | 1.057 | 4.52 | 4557 | 25 | 4585 | 50 | 4648 | 151 |
| | 2–2 | 62 | 55 | 16 | 0.29 | 0.5953 | 1.68 | 97.2 | 4.0 | 1.184 | 3.66 | 4497 | 24 | 4657 | 41 | 5035 | 129 |
| | 3–1 | 89 | 69 | 8 | 0.12 | 0.6232 | 1.10 | 106.7 | 4.0 | 1.241 | 3.88 | 4563 | 16 | 4751 | 41 | 5203 | 140 |
| | 3–2 | 130 | 120 | 13 | 0.11 | 0.6266 | 0.67 | 103.0 | 2.9 | 1.192 | 2.85 | 4571 | 10 | 4716 | 30 | 5060 | 101 |
| | 3–3 | 97 | 193 | 16 | 0.08 | 0.6213 | 0.76 | 102.5 | 2.7 | 1.197 | 2.64 | 4559 | 11 | 4711 | 28 | 5073 | 93 |
| | 4–1 | 82 | 35 | 7 | 0.21 | 0.6070 | 1.85 | 88.3 | 4.5 | 1.055 | 4.12 | 4525 | 27 | 4561 | 46 | 4643 | 138 |
| | 4–2 | 74 | 103 | 24 | 0.23 | 0.6286 | 1.07 | 98.8 | 2.9 | 1.140 | 2.72 | 4576 | 15 | 4674 | 30 | 4905 | 94 |
| | 4–3 | 73 | 85 | 11 | 0.13 | 0.6323 | 1.38 | 116.2 | 3.1 | 1.333 | 2.82 | 4584 | 20 | 4837 | 32 | 5461 | 105 |
| | 4–4 | 66 | 69 | 16 | 0.23 | 0.6062 | 1.44 | 91.9 | 3.5 | 1.100 | 3.23 | 4523 | 21 | 4601 | 36 | 4782 | 110 |
| | 5–1 | 61 | 75 | 45 | 0.60 | 0.5911 | 1.50 | 87.5 | 3.6 | 1.074 | 3.31 | 4486 | 22 | 4552 | 37 | 4701 | 111 |
| | 5–2 | 70 | 83 | 28 | 0.34 | 0.6014 | 1.29 | 94.1 | 3.9 | 1.134 | 3.63 | 4511 | 19 | 4625 | 39 | 4887 | 125 |
| | 6 | 108 | 47 | 1 | 0.02 | 0.5854 | 1.83 | 117.8 | 9.1 | 1.459 | 8.96 | 4472 | 26 | 4851 | 24 | 5800 | 352 |
| | 7 | 81 | 19 | 5 | 0.29 | 0.6034 | 2.84 | 101.1 | 10.5 | 1.215 | 10.10 | 4516 | 41 | 4697 | 74 | 5126 | 367 |

[*] Denotes radiogenic Pb relative to the CDT Pb as common-lead compositions ($^{206}Pb/^{204}Pb = 9.307$, $^{207}Pb/^{206}Pb = 1.09861$, Tatsumoto et al., 1973).

Author's personal copy



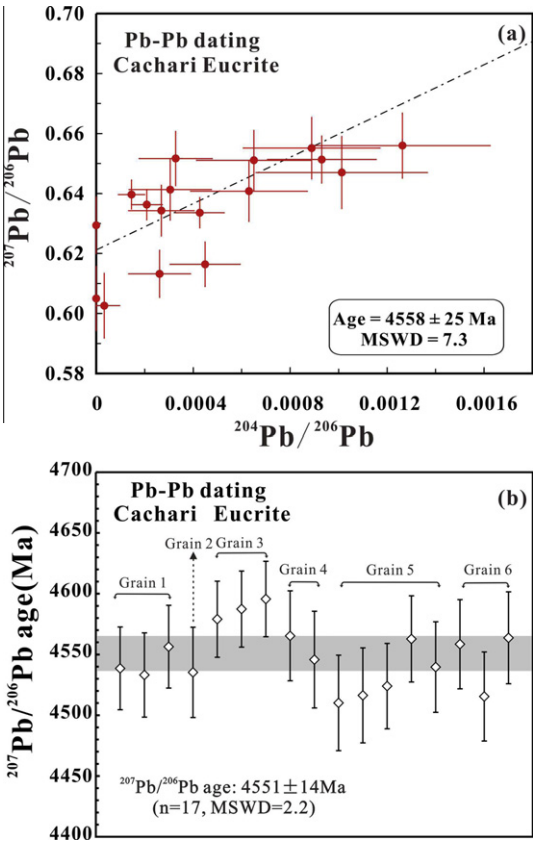


Fig. 7. Pb–Pb dating results for Cachari zircons determined by Cameca IMS-1280 SIMS in multi-collector mode (Table 1). (a) Correlation diagram between measured $^{204}Pb/^{206}Pb$ and $^{207}Pb/^{206}Pb$ ratios. (b) $^{207}Pb/^{206}Pb$ ages for Cachari zircons. The error bars of individual data point are $2\sigma$. The gray band shows the $2\sigma$ error of the weighted average $^{207}Pb/^{206}Pb$ age.

$^{207}Pb^*/^{206}Pb^*$ ages are summarized in Fig. 7. Zircons observed in the thin section are predominately ~5 μm or less in size, although a few are > 8 μm. Typically these zircons are anhedral with rounded (Fig. 1a, b and e) and irregular shapes (Fig. 1c and d). They are mostly associated with ilmenite (Fig. 1a, c and d), and occasionally accompanied by pyroxene (Fig. 1b) and plagioclase (Fig. 1e). Due to the multiple analyses on a small zircon ~5 μm or less, beam overlap could not be avoided during each analysis. Therefore, analytical depth may vary depending on how primary beam was moved at each analysis and the signal intensity of $^{90}Zr_2{}^{16}O_2$ and $^{206}Pb/^{204}Pb$ ratio would change accordingly.

Based on the measured $^{204}Pb/^{206}Pb$ and $^{207}Pb/^{206}Pb$ ratios in Table 1, a least-square regression of these data using Isoplot (Ludwig, 2003) gives an intercept of 0.621 ± 0.011, corresponding to a $^{207}Pb/^{206}Pb$ age of 4558 ± 25 Ma ($2\sigma$) (Fig. 7a). Using the CDT Pb isotope composition (Tatsumoto et al., 1973) as an estimate of the common-lead composition at the time of zircon crystallization, a weighted mean $^{207}Pb/^{206}Pb$ age of 4551 ± 14 Ma ($n = 17$, MSWD = 2.2) is obtained (Fig. 7b). This is similar to the results of Fig. 7a, indicating the low concentration of common-lead.

### 4.2. U–Pb dating results

$^{207}Pb/^{206}Pb$ age alone without U/Pb ratio is always prone to yield an apparently younger age if there was Pb loss at non-zero time in the past. To address this issue, in situ U–Pb dating is applied to check the concordance of the obtained Pb–Pb age. In situ U–Pb isotope data measured in Cachari, Béréba, Caldera, Camel Donga and Juvinas are listed in Table 2, and shown in U–Pb concordia diagrams (Fig. 8).

#### 4.2.1. Cachari

A total of three analyses were performed on zircon grain-7 in Cachari, which is enclosed within ilmenite with a size of 4 × 6 μm$^2$ (Fig. 1f). The concentrations of uranium and thorium for this zircon in Cachari are > 100 ppm and > 20 ppm, respectively. The Th/U ratio is ~0.2. The radiogenic $^{207}Pb/^{235}U$, $^{206}Pb/^{238}U$ and $^{207}Pb/^{206}Pb$ ratios of three analyses after common Pb correction range from 87.3 to 90.6, 1.03 to 1.06, and 0.6087 to 0.6224, respectively. The weighted average $^{207}Pb/^{235}U$, $^{206}Pb/^{238}U$ and $^{207}Pb/^{206}Pb$ ratio are of 88.9 (±3.3%), 1.044 (±2.9%) and 0.617 (±2.7%), corresponding to an age of 4568 ± 33 Ma ($2\sigma$), 4608 ± 96 Ma ($2\sigma$) and 4550 ± 39 Ma ($2\sigma$). In the U–Pb concordia diagram, three data points plot on the concordia and give a concordia age of 4548 ± 24 Ma (95% confidence, decay constant error was included) (Fig. 8a). This age is identical to the $^{207}Pb/^{206}Pb$ ages (obtained in both multicollection and monocollection mode), indicating that the U–Pb system of Cachari zircon was not disturbed during the late impact melting and/or thermal events.

#### 4.2.2. Béréba

A total of five analyses were performed on three zircon grains in Béréba. Zircons observed in the thin section are predominately 5~10 μm with rounded or irregular shapes. Grain-1 is ~15 × 10 μm in size and elliptical in shape and grain-2 is irregularly shaped with a size of 5 × 8 μm (Fig. 2a). Grain-3 is sub-rounded in shape and ~10 μm in size (Fig. 2b). The zircon grains are mostly associated with ilmenite (Fig. 2a), and occasionally accompanied by plagioclase (Fig. 2b). As shown in Table 2, zircons in Béréba show variable thorium concentrations from 11 to 112 ppm, but rather homogenous uranium contents of ~50 ppm. The Th/U ratio is also variable from 0.21 to 1.44. The radiogenic $^{207}Pb/^{235}U$, $^{206}Pb/^{238}U$ and $^{207}Pb/^{206}Pb$ ratios of five analyses after common Pb correction range from 77.1 to 95.2, 0.927 to 1.119 and 0.6029 to 0.6272, respectively. The weighted average $^{207}Pb/^{235}U$, $^{206}Pb/^{238}U$ and $^{207}Pb/^{206}Pb$ ratio are of 86 (±9.6%), 1.0 (±8%) and 0.618 (±1.4%), corresponding to an age of 4535 ± 96 Ma ($2\sigma$), 4483 ± 260 Ma ($2\sigma$) and 4522 ± 20 Ma ($2\sigma$). In the U–Pb concordia diagram, five data points are slightly reverse discordant and the chord intercepts the concordia at 4552 ± 21 Ma ($2\sigma$), which is exactly the same as the $^{207}Pb/^{206}Pb$ age of 4552 ± 20 Ma (Fig. 8b). This suggests U–Pb system remained as a closed in Béréba zircons since its formation.

Author's personal copy



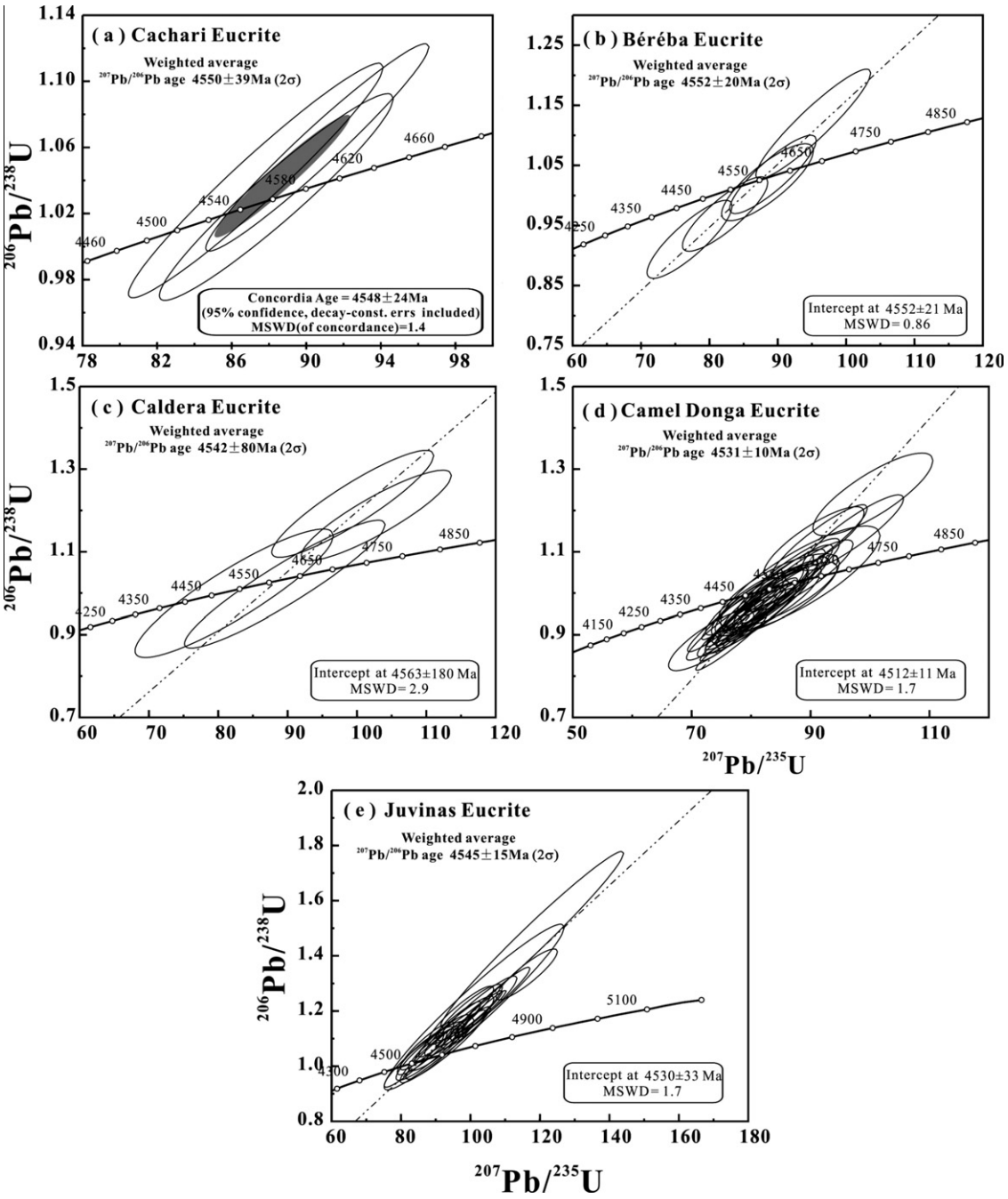


Fig. 8. U–Pb concordia diagram for zircon in Cachari, Béréba, Caldera, Camel Donga and Juvinas eucrites. Data-point error is 2$\sigma$. (a) Three data points of zircon grain-7 in Cachari plot on the concordia and give a concordia age of 4548 ± 24 Ma and $^{207}Pb/^{206}Pb$ age of 4550 ± 39 Ma (2$\sigma$). (b) Five data points for zircons in Béréba intercepts the concordia at 4552 ± 21 Ma and give $^{207}Pb/^{206}Pb$ age of 4552 ± 20 Ma (2$\sigma$). (c) Four data points for zircons in Caldera eucrite intercepts the concordia at 4563 ± 180 Ma and give $^{207}Pb/^{206}Pb$ age of 4542 ± 80 Ma (2$\sigma$). (d) Thirty-five data points for zircons in Camel Donga eucrite intercepts the concordia at 4512 ± 11 Ma and give $^{207}Pb/^{206}Pb$ age of 4531 ± 10 Ma (2$\sigma$). (e) Twenty data points for 7 zircon grains in Juvinas eucrite are slightly reverse discordant. The chord intercepts the concordia at 4530 ± 33 Ma and give $^{207}Pb/^{206}Pb$ age of 4545 ± 15 Ma (2$\sigma$).

*4.2.3. Caldera*

A total of four analyses were performed on a single zircon grain in Caldera. The zircon grain observed in this thin section was 8 × 12 μm in size, surrounded by ilmenite (Fig. 2c). The results are presented in Table 2. The concentration of uranium for the Caldera zircon are the lowest among the eucrite zircons in this study, ranging from 8 to 16 ppm. Th/U ratio is ~1.5–2.5. The radiogenic $^{207}Pb/^{235}U$, $^{206}Pb/^{238}U$ and $^{207}Pb/^{206}Pb$ ratios of five analyses after common Pb correction range from 82.3 to 102.8, 1 to 1.216, and 0.5925 to 0.6354, respectively. The weighted average $^{207}Pb/^{235}U$, $^{206}Pb/^{238}U$ and $^{207}Pb/^{206}Pb$

Author's personal copy



ratio are of 95 (±15%), 1.13 (±15%) and 0.613 (±5.6%), corresponding to an age of 4650 ± 150 Ma (2σ), 4894 ± 500 Ma (2σ) and 4542 ± 81 Ma (2σ). In the U–Pb concordia diagram, four data points intercept the chord at 4563 ± 180 Ma (2σ) (Fig. 8c).

#### 4.2.4. Camel Donga

A total of 35 analyses were performed on fourteen zircon grains in Camel Donga. Zircons are predominately less than 8 μm in size, occasionally more than 10 μm (Fig. 2e and f), with rounded and irregular shapes. They are mostly associated with ilmenite (Fig. 2e and f), and occasionally accompanied by plagioclase. Both of the uranium and thorium concentration for Camel Donga zircon are variable, ranging from 56 to 265 ppm and 5 to 441 ppm, respectively. Th/U ratio varies from 0.05 to 3.57. The radiogenic $^{207}Pb/^{235}U$, $^{206}Pb/^{238}U$ and $^{207}Pb/^{206}Pb$ ratios of five analyses after common Pb correction range from 73.3 to 100.5, 0.882 to 1.239, and 0.5849 to 0.6302, respectively. The weighted average $^{207}Pb/^{235}U$, $^{206}Pb/^{238}U$ and $^{207}Pb/^{206}Pb$ ratio are 82 (±2.2%), 0.98 (±2.4%) and 0.609 (±0.7%), corresponding to an age of 4492 ± 23 Ma (2σ), 4417 ± 79 Ma (2σ) and 4531 ± 10 Ma (2σ), respectively. In the U–Pb concordia diagram, data points intercept the chord at 4512 ± 11 Ma (2σ) (Fig. 8d), slightly younger than the other eucrites.

#### 4.2.5. Juvinas

A total of twenty analyses were performed on seven zircon grains in Juvinas. Zircons in this thin section are predominately ~10 μm or less in size with irregular shapes. They are mostly associated with ilmenite (Fig. 2h), and occasionally accompanied by plagioclase and pyroxene (Fig. 2g). The uranium and thorium concentrations for Juvinas zircon are variable, ranging from 19 to 193 ppm and 1 to 45 ppm. Th/U ratio is variable from 0.02 to 0.6. The radiogenic $^{207}Pb/^{235}U$, $^{206}Pb/^{238}U$ and $^{207}Pb/^{206}Pb$ ratios of twenty analyses after common Pb correction range from 83.8 to 117.8, 1.023 to 1.459, and 0.5854 to 0.6323, respectively. The weighted average $^{207}Pb/^{235}U$, $^{206}Pb/^{238}U$ and $^{207}Pb/^{206}Pb$ ratio are of 96.2 (±4%), 1.139 (±3.4%) and 0.615 (±1%), corresponding to an age of 4679 ± 48 Ma (2σ), 4915 ± 100 Ma (2σ) and 4545 ± 15 Ma (2σ). In the U–Pb concordia diagram, data points intercept the chord at 4530 ± 33 Ma (2σ) (Fig. 8e).

## 5. DISCUSSIONS

### 5.1. Crystallization ages of the non-cumulate eucrites

Previous studies have used numerous isotopic techniques (e.g., Ar–Ar, Pu–Xe, Rb–Sr, Sm–Nd and Pb–Pb mineral isochron) to date the eucrites in order to explore their thermal processes and evolutionary history of their parent body (Manhes et al., 1975; Birck and Allègre, 1978; Bogard et al., 1985; Carlson et al., 1988; Shukolyukov and Begemann, 1996a; Tera et al., 1997; Miura et al., 1998). Many of these isotopic systems were disturbed (see Section 2), which partly due to the relatively high degree of shock metamorphism (Boctor et al., 1987; Palme et al., 1988). Bukovanská and Ireland (1993) obtained a mixing line between ~4.56 Ga with common Pb (a $^{207}Pb/^{206}Pb$ of 0.4), with the lowest apparent $^{207}Pb/^{206}Pb$ age of ~4.2 Ga for Cachari, while for Béréba they obtained 4534 ± 16 Ma. They argued that the zircon U–Pb isotopic system of Cachari had been disturbed due to its small size, and that the disturbed zircon grain boundaries might contain a mixture of diffused radiogenic Pb and meteoritic common Pb (Bukovanská et al., 1996). Furthermore, they pointed out that a compromise must be made between spatial resolution of the primary beam and obtaining sufficient Pb signal for adequate precision when a small zircon grain was analyzed. With a spot size of nearly ~10 μm, Misawa et al. (2005) examined zircon grains in sixteen samples of eucrite and only identified five eucrites satisfying the spot size suitable for SHRIMP analysis. To overcome this limitation, we used Cameca IMS-1280 with spot size of 3–4 μm to guarantee both spatial resolution and adequate Pb signal.

For Cachari, the weighted average $^{207}Pb/^{206}Pb$ age of 4551 ± 14 Ma obtained in multicollection mode (Fig. 7),

Table 3
U–Pb and $^{207}Pb$-$^{206}Pb$ age summary of zircons from non-cumulate eucrite.

| Sample | Method | $^{207}Pb/^{206}Pb$ Age (Ma) | 2σ | Machine | Spot size | References |
|---|---|---|---|---|---|---|
| Vaca Muerta (VM-2)[a] | U–Pb | 4563 | 15 | SHRIMP-I | N/A | Ireland and Wlotzka (1992) |
| Pomozdino | U–Pb | 4560 | 5 | SHRIMP-II | 30 μm | Ireland and Bukovanská (2003) |
| Asuka 881388 | U–Pb | 4555 | 54 | SHRIMP-II | ~10 μm | Misawa et al. (2005) |
| Asuka 881467 | U–Pb | 4555 | 13 | SHRIMP-II | ~10 μm | Misawa et al. (2005) |
| Padvarninkai | U–Pb | 4553 | 13 | SHRIMP-II | ~10 μm | Misawa et al. (2005) |
| Yamato 75011 | U–Pb | 4550 | 9 | SHRIMP-II | ~10 μm | Misawa et al. (2005) |
| Yamato 792510 | U–Pb | 4545 | 15 | SHRIMP-II | ~10 μm | Misawa et al. (2005) |
| Cachari | $^{207}Pb$–$^{206}Pb$ | 4551 | 13 | CAMECA-1280 | ~3–4 μm | This study |
| Béréba | U–Pb | 4552 | 20 | CAMECA-1280 | ~3–4 μm | This study |
| Caldera | U–Pb | 4542 | 80 | CAMECA-1280 | ~3–4 μm | This study |
| Camel Donga | U–Pb | 4531 | 10 | CAMECA-1280 | ~3–4 μm | This study |
| Juvinas | U–Pb | 4545 | 15 | CAMECA-1280 | ~3–4 μm | This study |

[a] Vaca Muerta is a mesosiderite, but one of the two zircon grains, VM-2 was found in a eucritic clast, according to Ireland and Wlotzka (1992). The genetic link of mesosiderites to 4-Vesta parent body is demonstrated by their similar $\Delta^{17}O$ composition to that of HED (Greenwood et al., 2006).

Author's personal copy



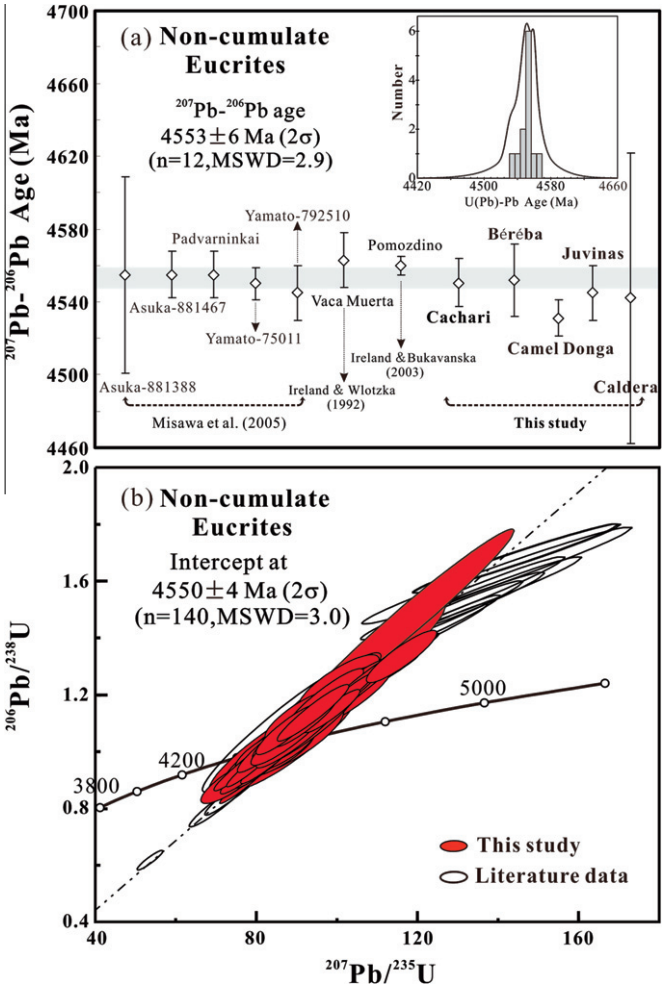


Fig. 9. (a) U–Pb and $^{207}$Pb/$^{206}$Pb age data for zircons from non-cumulate eucrite as summarized in Table 3. The error bars of individual data point are 2$\sigma$. The weighted average age is 4553 ± 6 Ma (2$\sigma$, 2 standard deviation of the population, shown by gray band). Probability density graph of non-cumulate eucrites is shown as inset to panel a. (b) U–Pb concordia diagram in basaltic eucrites (Vaca Muerta eucritic clast, Pomozdino, Asuka881388, Asuka881467, Padvaminkai, Y75011, Y792510, Cachari, Béréba, Caldera, Camel Donga and Juvinas. Data sources: Ireland and Wlotzka (1992), Ireland and Bukovanská (2003), Misawa et al. (2005), and this study. Data-point error ellipsoids are 2$\sigma$. The chord intercepts the concordia at 4550 ± 4 Ma (2$\sigma$), similar to the average age shown in panel a.

the weighted average $^{207}$Pb/$^{206}$Pb age of 4550 ± 39 Ma in mono-collection mode (Fig. 8a), and the U–Pb concordia age of 4548 ± 24 Ma (Fig. 8a) are practically identical (within 2$\sigma$ error) but significantly older than those previously obtained Ar–Ar, Pu–Xe, Sm–Nd and Pb–Pb mineral isochron ages for the same meteorite (Bogard et al., 1985; Shukolyukov and Begemann, 1996a; Tera et al., 1997). We argue that the new zircon ages probably represent the best estimation of the crystallization age of Cachari eucrite. This is entirely consistent with the zircon's high closure temperature of Pb (Lee et al., 1997).

Similarly, the U–Pb concordia age of zircons for Béréba in our study (4552 ± 21 Ma, Fig. 8b), indicating the primary crystallization age, is also older than the results from the other isotopoic systems, such as Rb–Sr (Manhes et al., 1975; Birck and Allègre, 1978), Pu–Xe (Shukolyukov and Begemann, 1996a; Miura et al., 1998), K–Ar (Shukolyukov and Begemann, 1996b), and Pb–Pb (Carlson et al., 1988; Tera et al., 1997).

The unbrecciated Caldera, with its larger uncertainty of the $^{207}$Pb/$^{206}$Pb age of 4542 ± 80 Ma (Fig. 8c), largely due to lower U concentration, is consistent with the result of Pu–Xe, Sm–Nd and Mn–Cr isotopic systematics within analytical error (Wadhwa and Lugmair, 1996; Shukolyukov and Begemann, 1996a). As for the strongly shocked Camel Donga, the $^{207}$Pb/$^{206}$Pb age of 4531 ± 10 Ma (Fig. 8d) is still similar to other eucrites. Data points for zircons in Juvinas are slightly reverse discordant. The weighted average $^{207}$Pb/$^{206}$Pb age is 4545 ± 15 Ma, whereas the U–Pb concordia intercept age is 4530 ± 33 Ma (Fig. 8e). The U–Pb intercept ages and $^{207}$Pb/$^{206}$Pb ages are consistent within the analytical error for all samples investigated. Thus, we argue that there was no significant Pb-loss from the zircons at non-zero time. Age obtained from the U–Pb system of zircons is obviously older than the other isotopic systems, implying that both U–Pb and Pb–Pb ages for zircons in eucrites are insensitive to the thermal impact and most probably represent the crystallization age.

Author's personal copy



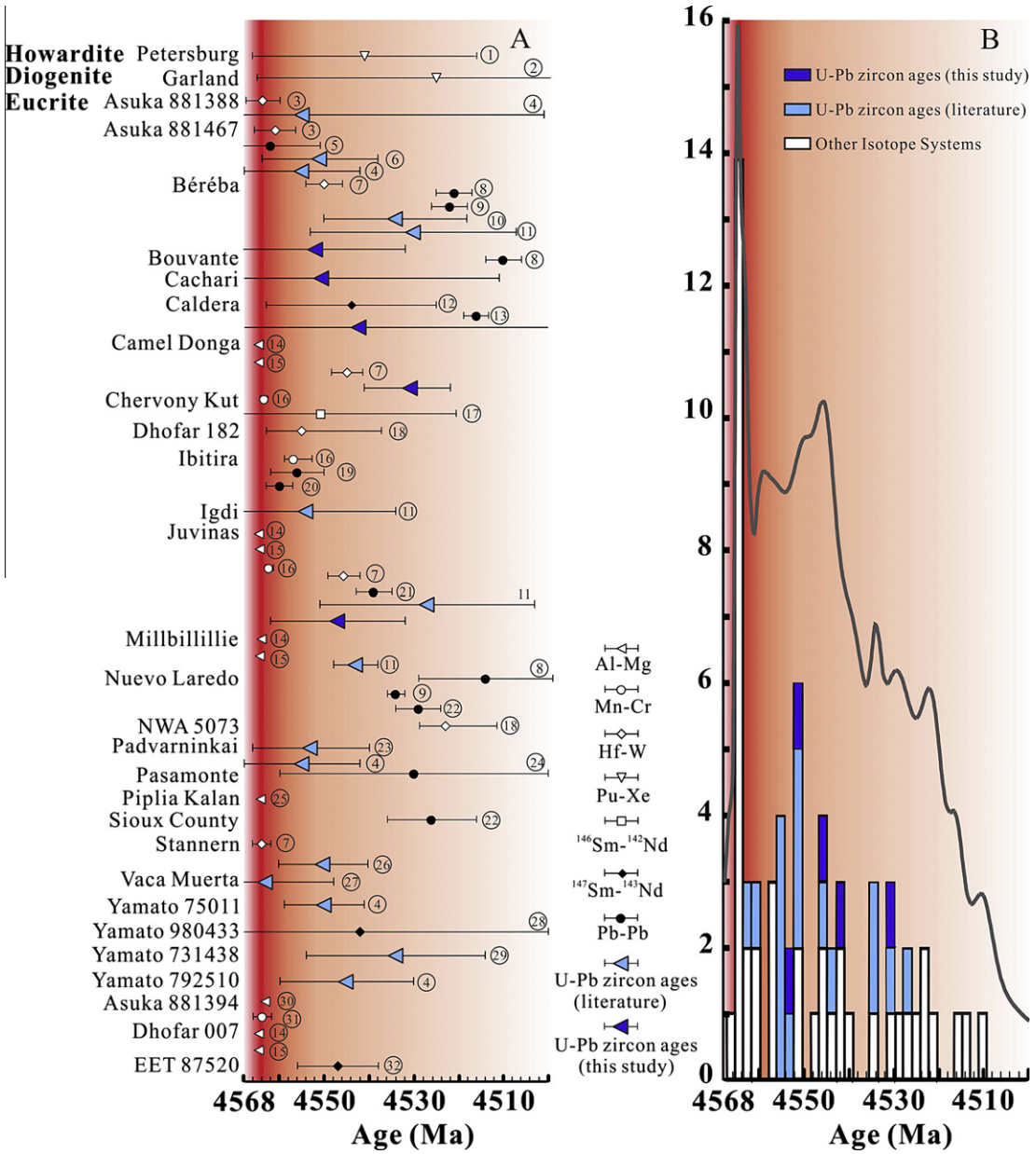


Fig. 10. (a) The chronological records of the first 50 Ma on Vesta based on radiometric age summary of HED meteorites, including one howardite (Petersburg), one diogenite (Garland) and 28 eucrites. Only high quality data with age uncertainty of less than 50 Ma are included. One of the two zircon grains found in a eucritic clast in Vaca Muerta (mesosiderite) according to Ireland and Wlotzka (1992) is also included. Shown in dark blue, solid horizontal triangles are U–Pb ages of zircons from this study. Light blue horizontal triangles are U–Pb zircon ages from literature. Open (white) symbols of various shapes are based on short-lived chronometers, whereas solid symbols of various shapes are based on long-lived chronometers. The data sources are: (1) Shukolyukov and Begemann (1996a); (2) Michel and Eugster (1994); (3) Srinivasan et al. (2007); (4) Misawa et al. (2005); (5) Misawa and Yamaguchi (2001); (6) Srinivasan et al. (2004); (7) Kleine et al. (2005); (8) Tera et al. (1997); (9) Carlson et al. (1988); (10) Bukovanská and Ireland (1993); (11) Lee et al. (2009); (12) Wadhwa and Lugmair (1996); (13) Galer and Lugmair (1996); (14) Bizzarro et al. (2005); (15) Schiller et al. (2010); (16) Lugmair and Shukolyukov, (1998); (17) Wadhwa and Lugmair (1995); (18) Roszjar et al. (2012); (19) Chen and Wasserburg (1985); (20) Manhes et al. (1987); (21) Manhes et al. (1984); (22) Tatsumoto et al. (1973); (23) Bukovanská et al. (1991); (24) Unruh et al. (1977); (25) Srinivasan et al. (1999); (26) Ireland and Bukovanská (1992); (27) Ireland and Wlotzka (1992); (28) Nyquist et al. (2008); (29) Ireland et al. (1992); (30) Nyquist et al. (2003); (31) Wadhwa et al. (2009); (32) Lugmair et al. (1991). (b) Histogram and the probability density curve (Ludwig, 2003) of the same age data shown in panel a, showing the intensities and diminishing magmatic activities on Vesta during the first 50 Ma. Red backgrounds symbolize the evolving intensities of magmatic activities on Vesta, as revealed by the available chronological data. (For interpretation of the references to color in this figure legend, the reader is referred to the web version of this article.).

Author's personal copy



Table 4
Constants used for thermal modeling.

| Description | Symbol | Value | Units |
|---|---|---|---|
| Density of rock | $\rho_{rock}$ | 3000 | kg m$^{-3}$ |
| Density of Fe-rich core | $\rho_{core}$ | 7874 | kg m$^{-3}$ |
| Density of water ice | $\rho_{H_2O\ ice}$ | 917 | kg m$^{-3}$ |
| Density of liquid water | $\rho_{liquid\ H_2O}$ | 1000 | kg m$^{-3}$ |
| Thermal diffusivity of silicate rock | $\kappa_{silicate}$ | $3.02 \times 10^{-7} + 2.78 \times 10^{-4}/T$ | m$^2$ s$^{-1}$ |
| Thermal diffusivity of Fe core | $\kappa_{core}$ | $5 \times 10^{-5}$ | m$^2$ s$^{-1}$ |
| Thermal diffusivity of amorphous water ice | $\kappa_{am}$ | $3.13 \times 10^{-7}$ | m$^2$ s$^{-1}$ |
| Thermal diffusivity of crystalline water ice | $\kappa_{xstl}$ | $(0.465 + 0.488/T)/(7039.8)$ | m$^2$ s$^{-1}$ |
| Thermal diffusivity of liquid water | $\kappa_{liquid\ H_2O}$ | $(-7.93 \times 10^{-6}\ T^2 + 0.00634T - 0.581)/(4.186 \times 10^6)$ | m$^2$ s$^{-1}$ |
| Specific heat of water ice | $c_{H_2O\ ice}$ | $7.49T + 90$ | J kg$^{-1}$ K$^{-1}$ |
| Specific heat of liquid water | $c_{liquid\ H_2O}$ | $4.187 \times 10^3$ | J kg$^{-1}$ K$^{-1}$ |
| Specific heat of silicate | $c_{silicate}$ | 1050 | J kg$^{-1}$ K$^{-1}$ |
| Specific heat of Fe-rich core | $c_{core}$ | 450 | J kg$^{-1}$ K$^{-1}$ |
| Heat production due to $^{26}$Al decay | $Q_{^{26}Al}$ | 0.45958 | W/(kg $^{26}$Al) |
| Heat production due to $^{60}$Fe decay | $Q_{^{60}Fe}$ | $5.5814 \times 10^{-3}$ | W/(kg $^{60}$Fe) |
| Mass concentration of Al in initial rock | $A_{Al}$ | $1.18 \times 10^{-2}$ | kg $^{27}$Al/(kg rock) |
| Mass concentration of Fe in initial rock | $A_{Fe}$ | 0.211 | kg $^{56}$Fe/(kg rock) |
| Initial $^{26}$Al/$^{27}$Al of body | $(^{26}Al/^{27}Al)_o$ | $5.2 \times 10^{-5}$ | |
| Initial $^{60}$Fe/$^{56}$Fe of body | $(^{60}Fe/^{56}Fe)o$ | $1.0 \times 10^{-7}$ | |
| Enthalpy of melting silicate | $\Delta H_{silt\ melt}$ | $4.0 \times 10^5$ | J kg$^{-1}$ |
| Enthalpy of melting Fe-rich core | $\Delta H_{core\ melt}$ | $2.7 \times 10^5$ | J kg$^{-1}$ |
| Enthalpy of amorphous–crystalline transition in water ice | $\Delta H_{xstln}$ | $-9.0 \times 10^4$ | J kg$^{-1}$ |
| Enthalpy of sublimation of water ice | $\Delta H_{sub}$ | $2.8 \times 10^6$ | J kg$^{-1}$ |
| Enthalpy of melting water ice | $\Delta_{H_2O\ melt}$ | $3.3 \times 10^5$ | J kg$^{-1}$ |
| Solidus for silicate | $T_{solidus,\ sil\ melt}$ | $1500 + 3.333$ h(km) | K |
| Solidus for Fe-rich core | $T_{solidus,\ core\ (Fe–S\ eutectic)}$ | 1260 K | K |
| Melting temperature of water | $T_{H_2O\ melt}$ | 273 | K |
| Amorphous–crystalline transition temperatures | $T_{am\text{-}xstln}$ | 130–273 | K |
| Water ice sublimation temperature range | $T_{sub}$ | 180–273 | K |
| Initial and surface temperature | $T_S$ | 180 | K |

Data source used in this table: Kallemeyn and Wasson (1981), Robertson (1988), Grimm and McSween (1989), Ghosh and McSween (1998), Prialnik and Podolak (1999), Lodders (2003), Prialnik et al. (2004) and Andrault et al. (2011).

We have summarized the published U–Pb and Pb–Pb zircon age data (Ireland and Wlotzka, 1992; Ireland and Bukovanská, 2003; Misawa et al., 2005) in Table 3 and shown in Fig. 9a and b. No correlation is observed between the U–Pb age and metamorphic degree of the samples. The weighted average $^{207}$Pb/$^{206}$Pb age is $4553 \pm 6$ Ma ($2\sigma$) as shown in Fig. 9a. The concordia intercept age is $4550 \pm 4$ Ma (Fig. 9b). We infer that the $4552 \pm 7$ Ma records major peak of basaltic magmatism of the eucrite parent body, *ca.* 8–20 Ma after the first solids, the Ca–Al-rich inclusions (CAIs) formation in the Solar System (Amelin et al., 2010; Connelly et al., 2012).

### 5.2. Magmatic records and the thermal model of the first 50 Ma on Vesta

Eucrite ages provide important constraints on several aspects of its parent body evolutionary history, in particular on the timing of its formation, and the ages of subsequent igneous, metamorphic and thermal overprinting. The former can be constrained by short-lived chronometers such as Hf–W, Mn–Cr and Al–Mg clocks, whereas the latter can be precisely determined using a suitable long-lived isotopic dating techniques such as U–Pb, Pb–Pb, $^{147}$Sm–$^{143}$Nd chronometers. Fig. 10 summarizes the first 50 Ma (post-CAI) of age data obtained for variety of HED meteorites, including U–Pb zircon age data from this study and other literature data.

Applying the short-lived $^{53}$Mn–$^{53}$Cr chronometer to a suite of whole rock samples of HEDs, and by comparing the calculated $^{53}$Mn/$^{55}$Mn ratio for HEDs with that of the angrite LEW 86010 (Pb–Pb age = $4557.84 \pm 0.52$ Ma) (Lugmair and Galer, 1992), a $^{53}$Mn-$^{53}$Cr age of $4564.8 \pm 0.9$ Ma was obtained by Lugmair and Shukolyukov (1998, 2001). Recently, a similar age of $4564.9 \pm 1.1$ Ma was obtained by Trinquier et al. (2008). This age is only $2.2 \pm 1.1$ Ma younger than the CAI formation (Amelin et al., 2010), suggesting that accretion, core formation, mantle differentiation and the first basalt formation on the eucrite parent body (EPB), widely thought to be

Author's personal copy



asteroid 4 Vesta, started very early (Lugmair and Shukolyukov, 1998, 2001; Yin et al., 2002; Trinquier et al., 2008). Similarly, $^{26}$Al–$^{26}$Mg system also indicates that the primary differentiation event of the eucrite parent body took place less than 4 Ma after CAI formation (Srinivasan et al., 1999; Bizzarro et al., 2005). In terms of the $^{182}$Hf–$^{182}$W system, Yin et al. (2002) concluded that the core formation of the eucrite parent body took place ~3 Ma after CAI formation and argued that this timescale is entirely consistent with the $^{53}$Mn (Lugmair and Shukolyukov, 1998) and $^{26}$Al constraints (Srinivasan et al., 1999). Yin et al. (2002) further argued that evolved initial $^{182}$W isotope composition of the eucrite isochron requires that the time of eruption of these basalts onto the surface of the EPB must post-dates core formation in 4 Vesta. The Hf-W constraints on core formation of 4 Vesta were latter relaxed to $3 \pm 6$ Ma after CAI formation (Kleine et al., 2004, 2009; Touboul et al., 2008).

All these data indicate that the core–mantle differentiation of the eucrite parent body took place at ~4564 ± 2 Ma (Fig. 10). However, without doubt, the magmatic activities on Vesta are protracted for much longer period of time on this dwarf planet. The varieties of crystallization ages of HED lithologies clearly postdate the peak thermal event of the global magma ocean (Greenwood et al., 2005) at 4564 ± 2 Ma (Fig. 10b). Zircons and other minerals are continuously crystallizing from basaltic magmas for the next 50 Ma and beyond. They represent discrete events well resolved from the global magma ocean event at 4564 ± 2 Ma. While the igneous activities on the Eucrite Parent Body (EPB) clearly started shortly after its metal–silicate differentiation at ~4564 Ma, there is even an indication of intensified activities ca. 8–20 Ma after the solar system formation, and gradually diminishing ever since (Fig. 10b).

How a small body such as Vesta, with radius of only ~260 km could retain the heat and sustain the magmatic activities for over 50 Ma is puzzling. The cumulate eucrites, although not a subject of this study (not included in Fig. 10), is known to be even younger (<4500 Ma) than most of the basaltic eucrites (e.g. Jacobsen and Wasserburg, 1984; Tera et al., 1997). It is unlikely that the all the younger ages are due to thermal metamorphism or late impact resetting. To understand the thermal history of Vesta and how this dwarf planet could have maintained the magmatic activities over 50 Ma, we have performed the following thermal model for Vesta.

### 5.3. Thermal modeling of Vesta

We solved the equation for conductive heat transfer in a sphere of radius $r$ with internal heat production $Q$.

$$\frac{\partial T}{\partial t} = \kappa\left(\frac{\partial^2 T}{\partial r^2} + \frac{2}{r}\frac{\partial T}{\partial r}\right) + (1-\phi)\frac{Q}{c} \quad (1)$$

where $\kappa$ is the thermal diffusivity, $c$ is the effective heat capacity, $\varphi$ is the volumetric fraction of the body initially composed of ice (water ice in this case), and $T$ is temperature. For a bone dry object like Vesta, we set $\varphi = 0$, or to a very small number. Eq. (1) is solved using explicit finite difference. The surface boundary condition is a fixed temperature of 170 K (not too dissimilar from the present-day steady-state mean surface temperature of Vesta). The initial condition is one of instantaneous accretion at an initial temperature of 170 K. The heat production term $Q$ is derived from the decay of $^{26}$Al and $^{60}$Fe. We used an initial atomic $^{26}$Al/$^{27}$Al of $5.2 \times 10^{-5}$, a mass of $^{27}$Al per kg of rock of $11.8 \times 10^{-3}$, an initial $^{60}$Fe/$^{56}$Fe of $1.0 \times 10^{-7}$, and a $^{56}$Fe/kg rock of 0.211 (i.e., chondritic concentrations of Al and Fe). Other parameters used in these calculations are summarized in Table 4 and obtained from a variety of literature sources (See Table 4 caption).

We included the thermal effects of melting of rock. The rock solidus is expressed as $T_{\text{solidus}} = 1500 + 0.87h$ where $h$ is depth below the surface in km. This equation is a reasonable linear approximation for the solidus for chondrites as shown by Andrault et al. (2011). The melting reaction progress variable at any given position and time step in the model is calculated as

$$\xi_{\text{sil melt}} = \frac{C_{\text{silicate}}(T - T_{\text{solidus}})}{\Delta H_{\text{sil melt}}} \quad (2)$$

Here, complete melting corresponds to $\xi = 1$ and no melting corresponds to $\xi = 0$. Eq. (2) accounts for the multivariate (i.e., polythermal at fixed pressure) nature of both rock melting and crystallization from melt. For example, with the constants used in our calculations (Table 4), the liquidus implied by Eq. (2) at $h = 100$ km is 1968 K, or 381 K above the solidus. This temperature interval of melting is generally consistent with detailed models for melting of chondrites at low and moderate pressures (Andrault et al., 2011).

Water and its phase changes can be an important heat sink/source and so we also included phase changes in water, including the irreversible transitions from amorphous to crystalline ice upon heating, reversible ice to liquid, and ice and liquid to vapor. Reaction progress variables for the three water phase transitions are

$$\begin{aligned}
\xi_{\text{H}_2\text{O}_{\text{melting}}} &= \sum_i \frac{c_{\text{H}_2\text{O}_i}(T_i - 270)}{\Delta H_{\text{H}_2\text{O}_{\text{melting}}}} \\
\xi_{\text{H}_2\text{O}_{\text{xstln}}} &= \sum_i \frac{c_{\text{H}_2\text{O}_i}(130 - T_i)}{\Delta H_{\text{xstln}}} \\
\xi_{\text{sub}} &= \sum_i \frac{c_{\text{H}_2\text{O}_i}(T_i - 180)}{\Delta H_{\text{sub}}}
\end{aligned} \quad (3)$$

The melting/solidification transition is univariant in temperature–pressure space and so is effectively isothermal at a given location in the body. Therefore the reaction progress variables for these phase changes are summations (positive for melting, negative for crystallization) over time steps $i$ at each location in the body where temperatures are near the melting/solidification temperature of 273 K as a result of thermal buffering by the enthalpy effects of melting and solidification (see discussion of heat capacities, below). The sublimation of ice is a potentially important heat sink during the earliest evolution of wet planetesimals. The details of this process depend critically on gas permeability, a parameter that is largely unknown (Gounelle et al., 2008); where gas permeability is limited, partial pressure of water in communication with water ice rapidly

Author's personal copy



equilibrates and there can be no sublimation. Eq. (3) yields small degrees of sublimation continuing from 180 K to the melting point of water.

Enthalpies of phase transitions are accommodated at each location $i$ and each time step through the specific heat in Eq. (1). Upon heating, the specific heat is calculated using

$$\begin{aligned} c_i = 1050 &+ \left(\frac{\Delta H_{\text{sil melt}}}{\Delta T_{\text{sil melt}}}\right)\int_{\xi_{\text{sil melt},i}=0}^{\xi_{\text{sil melt},i}=1}(1-\xi_{\text{sil melt},i})\delta(\xi_{\text{sil melt}}-\xi_{\text{sil melt},i})d\xi_{\text{sil melt}} \\ &+ \left(\frac{\Delta H_{\text{xstln}}}{\Delta T_{\text{xstln}}}\right)\left(\frac{\phi}{1-\phi}\right)\frac{\rho_{\text{ice}}}{\rho_{\text{rock}}} \\ &\times \int_{\xi_{\text{xstln}}=0}^{\xi_{\text{xstln}}=1}(1-\xi_{\text{xstln},i})\delta(\xi_{\text{xstln}}-\xi_{\text{xstln},i})d\xi_{\text{xstln}} \\ &+ \left(\frac{\Delta H_{\text{sub}}}{\Delta T_{\text{sub}}}\right)\left(\frac{\phi}{1-\phi}\right)\frac{\rho_{\text{ice}}}{\rho_{\text{rock}}} \\ &\times \int_{\xi_{\text{sub},i}=0}^{\xi_{\text{sub},i}=1}(1-\xi_{\text{sub},i})\delta(\xi_{\text{sub}}-\xi_{\text{sub},i})d\xi_{\text{sub}} \\ &+ \left(\frac{\Delta H_{\text{H}_2\text{O melt}}}{\Delta T_{\text{H}_2\text{O melt}}}\right)\left(\frac{\phi}{1-\phi}\right)\frac{\rho_{\text{H}_2\text{O}}}{\rho_{\text{rock}}} \\ &\times \int_{\xi_{\text{H}_2\text{O melt},i}=0}^{\xi_{\text{H}_2\text{O melt},i}=1}(1-\xi_{\text{H}_2\text{O melt},i})\delta(\xi_{\text{H}_2\text{O melt}}-\xi_{\text{H}_2\text{O melt},i})d\xi_{\text{H}_2\text{O melt}} \end{aligned} \tag{4}$$

and upon cooling the expression is

$$\begin{aligned} c_i = 1050 &- \left(\frac{\Delta H_{\text{sil melt}}}{\Delta T_{\text{sil melt}}}\right)\int_{\xi_{\text{sil melt},i}=0}^{\xi_{\text{sil melt},i}=1}\xi_{\text{sil melt},i}\delta(\xi_{\text{sil melt}}-\xi_{\text{sil melt},i})d\xi_{\text{sil melt}} \\ &- \left(\frac{\Delta H_{\text{H}_2\text{O melt}}}{\Delta T_{\text{H}_2\text{O melt}}}\right)\left(\frac{\phi}{1-\phi}\right)\frac{\rho_{\text{H}_2\text{O}}}{\rho_{\text{rock}}} \\ &\times \int_{\xi_{\text{H}_2\text{O melt},i}=0}^{\xi_{\text{H}_2\text{O melt},i}=1}\xi_{\text{H}_2\text{O melt},i}\delta(\xi_{\text{H}_2\text{O melt}}-\xi_{\text{H}_2\text{O melt},i})d\xi_{\text{H}_2\text{O melt}} \end{aligned} \tag{5}$$

where 1050 is the specific heat for rock in J/(kg k), the enthalpies of transition, temperature intervals of transition, and densities are represented by the usual symbols, $\rho_{H2O}$ is the density of the reactant phase of water, and the amorphous to crystalline ice transition and sublimation are treated as irreversible. For univariant reactions involving water the $\Delta T$ is taken to be three degrees (a numerical expediency justified on the basis of a small degree of reaction overstepping). The other $\Delta T$ values are defined by Eq. (3). Reaction progress variables in Eqs. (4) and (5) account for depletion of the reactant phase during the transitions, although the results are not sensitive to accounting for this depletion. The integrals of the form

$$\int_{\xi_i=0}^{\xi_i=1} f(\xi_i)\delta(\xi-\xi_i)d\xi = \begin{cases} f(\xi_i) & if \quad 0<\xi_i<1 \\ 0 & \text{for all other values for } \xi \end{cases} \tag{6}$$

in Eqs. (4) and (5) are Dirac measures ($\delta$ is the Dirac delta function) of reaction progress at a location $i$ in the system that evaluate to $f(\xi_i)$, i.e. $1-\xi_i$ or $\xi$, when $0<\xi_i<1$ and 0 for all other values of $\xi_i$. This is an economical way of expressing the condition that enthalpy effects of the four phase transitions apply during the respective transition temperatures only.

Thermal diffusivities are calculated from the weighted contributions of rock, rock melt, and the various phases of water:

$$\begin{aligned} &\kappa = \phi\kappa_{\text{H}_2\text{O}} + (1-\phi)\kappa_{\text{rock}} \\ &\kappa_{\text{rock}} = \kappa_{\text{solid rock}}Nu, \quad \xi_{\text{sil melt}} > 0.1 \\ &\kappa_{\text{H}_2\text{O}} = \xi_{\text{H}_2\text{O melt}}\kappa_{\text{H}_2\text{O,liq}} + \left(1-\xi_{\text{H}_2\text{O melt}}\right)\kappa_{\text{ice}} \\ &\kappa_{\text{ice}} = \xi_{\text{H}_2\text{O xstln}}\kappa_{\text{xstl}} + \left(1-\xi_{\text{H}_2\text{O xstln}}\right)\kappa_{\text{am}} \end{aligned} \tag{7}$$

where $\kappa_{\text{am}}$ is the thermal diffusivity of amorphous solid water and we have neglected the thermal diffusivity of the vapor phase.

In order to account for enhanced heat flux to the surface due to convection of silicate melt the effective $\kappa$ for the molten rock with $0<\xi_{\text{sil melt}}\leqslant 1$ was enhanced by the Nusselt number, $Nu$, where $Nu$ is the ratio of actual heat transfer to purely conductive heat transfer such that $\kappa_{\text{actual}} = \kappa Nu$. We adopted a single value of 100 for $Nu$. This value is intermediate between maxima with 100% melt and much lower values with lower melt fractions.

Differentiation of Vesta will have had profound effects on its thermal history. This is because the primary heat source, $^{26}$Al, is redistributed away from the center of the body and towards the surface as a consequence of the differentiation process. Migration of $^{26}$Al towards the surface leads to a greater heat loss. We have considered the consequences of expulsion of $^{26}$Al from the core of the body as it forms. We find that the effects of core formation on the longevity of melting of the mantle are profound.

We produced a simple simulation of rapid core formation (e.g., Gupta and Sahijpal, 2010) by specifying a replacement of chondritic rock with an iron rich alloy when $\xi_{\text{sil melt},i}$ exceeds 0.8. The mass of Fe required to replace the original silicate rock is extracted uniformly from the above material, simulating sinking of Fe and accumulation in regions of high melt fraction (accumulation starts at the center of the body progressing rapidly outward). In the simulations presented here, the core forms in $10^4$ years. Thermal properties, including heat production, are modified to match those for an Fe-rich core in the regions of core formation. The effects of removing a finite mass of Fe, including $^{60}$Fe, and increasing the concentrations of the remaining nuclides, including $^{26}$Al, are included by monitoring the mass of the core at each time step, subtracting this mass of Fe from the total remaining rock, and adjusting concentrations accordingly.

Thermal effects associated with differentiation alone are negligible. We demonstrate this by comparing the gravitational potential energy of differentiated and undifferentiated model Vestas. The latter is obtained from the expression

$$U_{\text{undiff}} = -\frac{3GM_o^2}{5R_o} \tag{8}$$

where $M_o$, the mass of our model Vesta assuming a density $\rho_o$ of 3000 kg/m$^3$ and a radius $R_{\text{o}}$ of 265 km, is $2.3\times10^{20}$ kg. The resulting potential energy is $-8.0\times10^{24}$ J. The differentiated Vesta will have a gravitational potential energy of

$$U_{\text{differ}} = U_{\text{undiff}} - U_{\text{sil core}} + U_{\text{Fe core}} \tag{9}$$

Author's personal copy



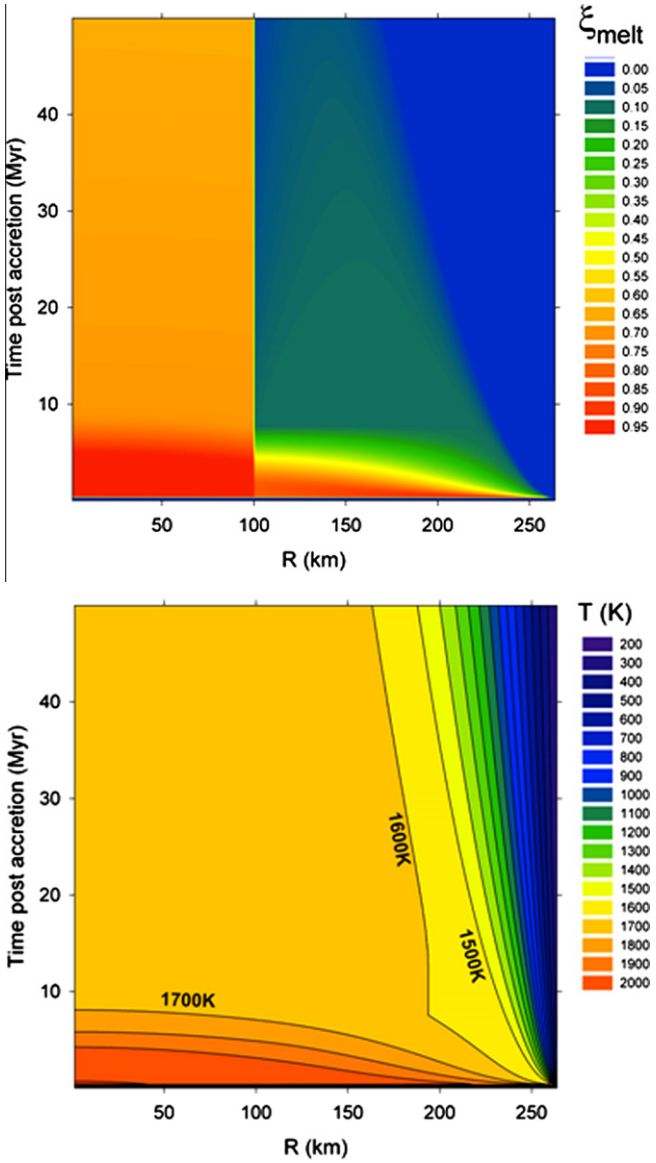


Fig. 11. Thermal modeling of Vesta for its first 50 Ma since accretion. (a) Melt fraction in the interior of the Vesta. The 100 km boundary divides Vesta's metallic core (Russell et al., 2012) from the silicate mantle. (b) Temperature distribution in the interior of Vesta. The "blue" region represents largely solidified Vesta's crust. The source of basaltic eucrites was presumably beneath the bottom of the crust where the melt fraction > 5% and temperature > 1500 K. Parameters used in the model are detailed in Table 4. Accretion at 0.3 Ma post CAI is assumed in this model for Vesta, consistent with the mean time of accretion $< t > = 0.8 \pm 0.8$ Ma for Vesta with fully accreted mass by $\sim 3$ Ma, based on currently available best constraints on Hf–W isotopic systematics of eucrites (*c.f.* Fig. 6 in Jacobsen, 2005).

Using Eq. (3) and a mass for the 100 km radius Fe core (Russell et al., 2012) of $3.3 \times 10^{19}$ kg and a core density of 7900 kg/m$^3$ yields a difference in potential energy $U_{\text{undiff}} - U_{\text{diff}}$ of $1 \times 10^{24}$ J. This potential energy difference dissipated entirely as heat yields a temperature rise distributed throughout the body of $\Delta T \sim \Delta U / c_{\text{rock}} M_{\text{o}} = 4$°K. For this reason we neglect the dissipative heat associated with migration of Fe to the core. Eq. (8) also shows that the potential energy effects of accretion of Vesta are on the order of 50°K. An increase in the initial temperature of the body of this magnitude has no discernible impact on the final results.

We also include the effects of melting/solidification of the Fe-rich core using the specific heat and enthalpy of melting for iron metal (using the form of Eqs. (4) and (5)). We use a solidus of 1260 K for the Fe-rich core, corresponding to the Fe–S binary eutectic melting point at a mass fraction S/(S + Fe) of $\sim 0.32$. Eq. (2) applied to melting of the Fe core results in complete melting ($\xi_{\text{core}} = 1$) at 1866 K. The ratio of specific heat to enthalpy of melting is 0.00165 compared with the silicate value of ~0.0026 (varies with T). The lower melting point of the Fe–S alloy overwhelms the lower $c/\Delta H$ relative to chondrite, causing a higher melt fraction in the core than in the overlying silicate

Author's personal copy



mantle. Results in which we raise the core solidus (up to 1700 K, corresponding to congruent melting at a S mass fraction of 0.06) causes the core to solidify prior to the overlying mantle but has no significant influence on the melt fraction in the rocky mantle vs. radius and time distribution.

Our results show that Vesta had significant (>50%) melting for about 5–6 million years following accretion. More importantly in the context of this study, there have been a smaller degree of partial melt (>10%) that persisted in the mantle of Vesta for tens of millions of years (Fig. 11a) and Vesta's mantle remained hot (>1500 K, Fig. 11b) over this period. Given such a thermal state of the dwarf planet for the first 50 Ma, it is permissible that basaltic eucrites formed by the conventional rise of small discrete magma parcels into the outer portion of Vesta. Melt extraction and migration mechanism may not have been drastically dissimilar to those described by Wilson et al. (2008) and Moskovitz and Gaidos (2011). In summary, the magma generation and crystallization for the next ~50 Ma, as recorded by zircon and other isotopic systems in eucrites (Fig. 10), is entirely consistent and feasible per our model results (Fig. 11). Cumulate eucrites, as late fractional crystallization products, buried deeper in the base of the Vesta's lower crust, likely remained hot for extensive period of time, thus their isotopic system could have been closed after < 4500 Ma.

## 6. CONCLUSIONS

The high sensitivity technique described in this paper utilizes spot size of 3–4 μm with Cameca 1280 to perform Pb–Pb and U–Pb in situ dating of zircons with little loss of precision compared with the previous work performed on much larger zircon grains. We exploited a number of technical developments with the new instrument and a set of associated protocols to accomplish small spots analyses, with enhanced sensitivity, higher transmission, and stable signals for high precision. The features include: (1) Gaussian mode of primary beam of low intensity (0.1–0.2 nA); (2) oxygen bleeding with a gas pressure of $\sim 1 \times 10^{-5}$ torr into the sample chamber; (3) high magnification transfer settings of ~260; (4) nuclear magnetic resonance (NMR) controller to stabilize instrumental mass drift to less than 2.5 ppm in 16 h.

We applied the technique to a suite of small zircons found in five basaltic eucrites: Cachari, Béréba, Caldera, Camel Donga and Juvinas. The mean Pb–Pb age is found to be $4541 \pm 11$ Ma and the mean U–Pb concordia age is $4525 \pm 24$ Ma. The consistency between these ages suggests that there was insignificant Pb-loss in the zircons investigated. These ages most likely represent the crystallization age of the basaltic magma on the Vesta's surface. A synthesis of available modern chronological data indicate that eucrite parent body underwent initial core–mantle differentiation at ~4564 Ma, followed by peak basaltic magmatism at ~4552 Ma, which gradually diminished over the next 50 Ma. Our thermal modeling of Vesta suggests that melt fraction of > 10% with its interior temperature over 1500 K could be maintained for tens of millions years since its accretion, thus permitting a protracted magmatic activity on Vesta, as observed in HEDs.

## ACKNOWLEDGEMENTS

Q.-Z.Y. thanks Tim McCoy and Linda Welzenbach at the Smithsonian National Museum of Natural History for providing the Béréba, Cachari, Caldera, Camel Donga and Juvinas eucrite thin sections used in this study. We are indebted to Qian Mao and Wenjie Shen at IGG, CAS for their technical assistance with the BSE imaging, to Jing Chen at Peking University for her help with the SEM imaging of eucrite zircons prior to SIMS analyses. We sincerely acknowledge Alan Hicklin at the Spectral Imaging Facility of UC Davis for his help with the SEM and AFM images for the Béréba zircons. Discussions with Paul Warren and David W. Mittlefehldt about the origin of eucrites were most helpful. We thank Dr. Noriko Kita and the two anonymous reviewers and Associate Editor Dr. Janne Blichert-Toft for their constructive comments and editorial handling that have helped to substantially improve the manuscript. The work is supported in part by State Key Laboratory of Lithospheric Evolution, IGG-CAS Grants Z201003 and the NSFC "Group Innovation" grant (41221002).

## REFERENCES

Amelin Y., Kaltenbach A., Iizuka T., Stirling C. H., Ireland T. R., Petaev M. and Jacobsen S. B. (2010) U–Pb chronology of the Solar System's oldest solids with variable $^{238}U/^{235}U$. *Earth Planet. Sci. Lett.* **300**, 343–350.

Andrault D., Bolfank-Casanova N., Lo Nigro G., Bouhifd M. A., Garbarino G. and Mezouar M. (2011) Solidus and liquidus profiles of chondritic mantle: implication for melting of the Earth across its history. *Earth Planet. Sci. Lett.* **304**, 251–259.

Binzel R. P. and Xu S. (1993) Chips off of asteroid 4 Vesta: evidence for the parent body of basaltic achondrite meteorites. *Science* **260**, 186–191.

Birck J. L. and Allègre C. J. (1978) Chronology and chemical history of the parent body of basaltic achondrites studied by the $^{87}Rb$–$^{87}Sr$ method. *Earth Planet. Sci. Lett.* **39**, 37–51.

Bizzarro M., Baker J. A., Haack H. and Lundgaard K. L. (2005) Rapid timescales for accretion and melting of differentiated planetesimals inferred from $^{26}Al$–$^{26}Mg$ chronometry. *Astrophys. J. Lett.* **632**, L41–L44.

Boctor N. Z., Carlson R. W. and Tera F. (1987) Petrology and shock metamorphism of the monomict eucrites Cachari and Stannern (abstract). *Meteorit. Planet. Sci.* **22**, 332.

Bogard D. D. (1995) Impact ages of meteorites: a synthesis. *Meteoritics* **30**, 244–268.

Bogard D. D., Taylor G. J., Keil K., Smith M. R. and Schmitt R. A. (1985) Impact melting of the Cachari eucrite 3.0 Gy ago. *Geochim. Cosmochim. Acta* **49**, 941–946.

Buchanan P. C., Noguchi T., Bogard D. D., Ebihara M. and Katayama I. (2005) Glass veins in the unequilibrated eucrite Yamato 82202. *Geochim. Cosmochim. Acta* **69**, 1883–1898.

Bukovanská M. and Ireland T. R. (1993) Zircons in eucrites: pristine and disturbed U–Pb systematics (abstract). *Meteorit. Planet. Sci.* **28**, 333.

Bukovanská M., Ireland T. R., Goresy A. El., Palme H., Spettel B. and Wlotzka F. (1991) Zircons in the Padvarninkai brecciated eucrite (abstract). *Meteorit. Planet. Sci.* **26**, 325.

Bukovanská M., Ireland T. R. and Janicke J. (1996) Ion probe dating of some baddeleyites in Antarctic basaltic achondrites (abstract). *Meteorit. Planet. Sci.* **31**, 24.

Bukovanská M., Ireland T. R. and Janicke J. (1997) Zircons and baddeleyites from differentiated meteorites basaltic achondrites:

Author's personal copy



ion probe dating and REE systematics. *Meet. Assoc. Eur. Geol. Soc.* **10**, 20 (abstr.).

Carlson R. W., Tera F. and Boctor N. Z. (1988) Radiometric geochronology of the eucrites Nuevo Laredo and Béréba. *Lunar Planet. Sci. Conf. XIX*. pp. 166–167.

Chamberlain K. R., Schmitt A. K., Swapp S. M., Harrison T. M., Colberg N. S., Bleeker W., Peterson T. D., Jefferson C. W. and Khudoley A. K. (2010) In situ U–Pb SIMS (IN-SIMS) micro-baddeleyite dating of mafic rocks: method with examples. *Precambrian Res.* **183**, 379–387.

Chen J. H. and Wasserburg G. J. (1985) U–Th–Pb isotopic studies on meteorite ALHA81005 and Ibitira. *Lunar Planet. Sci. Conf. 16.* pp. 119–120.

Connelly J. N., Bizzarro M., Krot A. N., Nordlund Å., Wielandt D. and Ivanova M. A. (2012) The absolute chronology and thermal processing of solids in the solar protoplanetary disk. *Science* **338**, 651–655.

Drake M. J. (2001) The eucrite/Vesta story. *Meteorit. Planet. Sci.* **36**, 501–513.

Ducloux E. H. (1921) Piedra meteorica (aerolito) Cachari, Provincia de Buenos Aires. *Rev. Mus. La Plata* **25**, 118.

Ducloux E. H. (1928) Datos sobre la piedra meteorica de Cachari. *Rev. Fac. Quim. Farm. Univ Nac. La Plata* **5**, 13–15.

Fredriksson K. and Kraut F. (1967) Impact glass in the Cachari eucrite. *Geochim. Cosmochim. Acta* **31**, 1701–1704.

Galer S. J. G. and Lugmair G. W. (1996) Lead isotope systematics of noncumulate eucrites. *Meteorit. Planet. Sci.* **31**, A47–A48.

Ghosh A. and McSween H. Y. (1998) A thermal model for the differentiation of asteroid 4 Vesta, based on radiogenic heating. *Icarus* **134**, 187–206.

Gomes R., Levison H. F., Tsiganis K. and Morbidelli A. (2005) Origin of the cataclysmic Late Heavy Bombardment period of the terrestrial planets. *Nature* **435**, 466–469.

Gounelle M., Morbidelli A., Bland P. A., Spurny P., Young E. D. and Sephton M. (2008) Meteorites from the outer solar system? In *The Solar System Beyond Neptune* (eds. M. A. Barucci, H. Boehnhardt, D. P. Crukshank and A. Morbidelli). The University of Arizona Press, Tucson, pp. 525–541.

Greenwood R. C., Franchi I. A., Jambon A. and Buchanan P. C. (2005) Widespread magma oceans on asteroidal bodies in the early Solar System. *Nature* **435**, 916–918.

Greenwood R. C., Franchi I. A., Jambon A., Barrat J. A. and Burbine T. H. (2006) Oxygen isotope variation in stony-iron meteorites. *Science* **313**, 1763–1765.

Grimm R. E. and McSween H. Y. (1989) Water and the thermal evolution of carbonaceous chondrite parent bodies. *Icarus* **82**, 244–280.

Gupta G. and Sahijpal S. (2010) Differentiation of Vesta and the parent bodies of the other achondrites. *J. Geophys. Res.* **115**, E08001.

Heaman L. M. (2009) The application of U–Pb geochronology to mafic, ultramafic and alkaline rocks: an evaluation of three mineral standards. *Chem. Geol.* **261**, 43–52.

Ireland T. R. and Bukovanská M. (1992) Zircons from the Stannern eucrite (abstract). *Meteorit. Planet. Sci.* **27**, 237.

Ireland T. R. and Bukovanská M. (2003) Initial $^{182}Hf/^{180}Hf$ in meteoritic zircons. *Geochim. Cosmochim. Acta* **67**, 4849–4856.

Ireland T. R. and Wlotzka F. (1992) The oldest zircons in the solar system. *Earth Planet. Sci. Lett.* **109**, 1–10.

Ireland T. R. and Williams I. S. (2003) Considerations in zircon geochronology by SIMS. *Rev. Mineral. Geochem.* **53**, 215–241.

Ireland T. R., Saiki K. and Takeda H. (1992) Age and trace-element chemistry of Yamato 791438 ziron. *Lunar Planet. Sci. Conf. XXIII.* pp. 569–570 (abstr.).

Jacobsen S. B. (2005) The Hf–W isotopic system and the origin of the Earth and Moon. *Annu. Rev. Earth Planet. Sci.* **33**, 531–570.

Jacobsen S. B. and Wasserburg G. J. (1984) Sm–Nd isotopic evolution of chondrites and achondrites 2. *Earth Planet. Sci. Lett.* **67**, 137–150.

Kallemeyn G. W. and Wasson J. T. (1981) The compositional classification of chondrites – I. The carbonaceous chondrite groups. *Geochim. Cosmochim. Acta* **45**, 1217–1230.

Kaneoka I., Nagao K., Yamaguchi A. and Takeda H. (1995) $^{40}Ar$–$^{39}Ar$ analyses of Juvinas fragments. *Meteorites* **8**, 287–296.

Kitts K. and Lodders K. (1998) Survey and evaluation of eucrite bulk compositions. *Meteorit. Planet. Sci.* **33**, A197–A213.

Kleine T., Mezger K., Munker C., Palme H. and Bischoff A. (2004) $^{182}Hf$–$^{182}W$ isotope systematics of chondrites, eucrites and martian meteorites: chronology of core formation and early mantle differentiation in Vesta and Mars. *Geochim. Cosmochim. Acta* **68**, 2935–3946.

Kleine T., Mezger K., Palme H., Scherer E. and Munker C. (2005) The W isotope composition of eucrite metals: constraints on the timing and cause of the thermal metamorphism of basaltic eucrites. *Earth Planet. Sci. Lett.* **231**, 41–52.

Kleine T., Touboul M., Bourdon B., Nimmo F., Mezger K., Palme H., Jacobsen S. B., Yin Q. Z. and Halliday A. N. (2009) Hf–W chronology of the accretion and early evolution of asteroids and terrestrial planets. *Geochim. Cosmochim. Acta* **73**, 5150–5188.

Kurahashi E., Kita N. T., Nagahara H. and Morishita Y. (2008) $^{26}Al$–$^{26}Mg$ systematics of chondrules in a primitive CO chondrite. *Geochim. Cosmochim. Acta* **72**, 3865–3882.

Lacroix A. (1926) Eucrite de Cachari. *Archieves du Museum*, Paris 6E serie 1.

Lee J. K. W., Ian S., Williams I. S. and Ellis D. J. (1997) Pb, U and Th diffusion in natural zircon. *Nature* **390**, 159–162.

Lee S. R., Kim H., Cho D. L., Kenji H. and Hidaka H. (2009) U–Pb dating of zircons from eucrites: a preliminary report (abstract). *Geochim. Cosmochim. Acta* **73**, A737.

Li X. H., Liu Y., Li Q. L. and Guo C. H. (2009) Precise determination of phanerozoic zircon Pb/Pb age by multicollector SIMS without external standardization. *Geochem. Geophys. Geosyst.* **10**, Q04010.

Li Q. L., Li X. H., Liu Y., Tang G. Q., Yang J. H. and Zhu W. G. (2010) Precise U–Pb and Pb–Pb dating of phanerozoic baddeleyite by SIMS with oxygen flooding technique. *J. Anal. At. Spectrom.* **25**, 1107–1113.

Liu Y., Li X. H., Li Q. L., Tang G. Q. and Yin Q. Z. (2011) Precise U–Pb zircon dating at <5 micron scale by Cameca 1280 SIMS using Gaussian illumination probe. *J. Anal. At. Spectrom.* **26**, 845–851.

Lodders K. (2003) Solar system abundances and condensation temperatures of the elements. *Astrophys. J.* **591**, 1220–1247.

Ludwig K. R. (2003) Isoplot 3.00, a geochronological toolkit for Excel. *Berkeley Geochronology Center Special, Publication* No. 4.

Lugmair G. W. (1974) Sm–Nd ages: a new dating method. *Meteoritics* **9**, 369.

Lugmair G. W. and Galer S. J. G. (1992) Age and isotopic relationships among the angrites Lewis Cliff 86010 and Angra dos Reis. *Geochim. Cosmochim. Acta* **56**, 1673–1694.

Lugmair G. W. and Shukolyukov A. (1998) Early solar system timescales according to $^{53}Mn$–$^{53}Cr$ systematics. *Geochim. Cosmochim. Acta* **62**, 2863–2886.

Lugmair G. W. and Shukolyukov A. (2001) Early solar system events and timescale. *Meteorit. Planet. Sci.* **36**, 1017–1026.

Lugmair G. W., Galer S. J. G. and Carlson R. W. (1991) Isotope systematics of cumulate eucrite EET-87520. *Meteoritics* **26**, 368.

Manhes G., Tatsumoto M., Unruh D., Birck J. L. and Allegre C. J. (1975) Comparative $^{238}U$–$^{206}Pb$, $^{235}U$–$^{207}Pb$, $^{232}Th$–$^{208}Pb$,

Author's personal copy



$^{206}$Pb–$^{207}$Pb and $^{87}$Rb–$^{87}$Sr ages of basaltic achondrites and early evolution of the Solar System. *Lunar Planet. Sci. Conf.* p. 547.

Manhes G., Allegre C. J. and Provost A. (1984) U–Th–Pb Systematics of the eucrite Juvinas – precise age-determination and evidence for exotic lead. *Geochim. Cosmochim. Acta* **48**, 2247–2264.

Manhes G., Gopel C. and Allegre C. J. (1987) High-resolution chronology of the early solar-system based on lead isotopes. *Meteoritics* **22**, 453–454.

Marvin U. B. and Klein C. (1964) Meteoritic zircon. *Science* **146**, 919–920.

Michel T. and Eugster O. (1994) Primitive xenon in diogenites and plutonium-244-fission xenon ages of a diogenite, a howardite, and eucrites. *Meteoritics* **29**, 593–606.

Misawa K. and Yamaguchi A. (2001) U–Pb isotpic systematics of zircons from basaltic euctites. *Antarctic Meteorit.* **26**, 83–84.

Misawa K., Yamaguchi A. and Kaiden H. (2005) U–Pb and $^{207}$Pb-$^{206}$Pb ages of zircons from basaltic eucrites: Implications for early basaltic volcanism on the eucrite parent body. *Geochim. Cosmochim. Acta* **69**, 5847–5861.

Miura Y. N., Nagao K., Sugiura N., Fujitani T. and Warren P. H. (1998) Noble gases, $^{81}$Kr–Kr exposure ages and $^{244}$Pu–Xe ages of six eucrites, Béréba, Binda, Camel Donga, Juvinas, Millbillillie and Stannern. *Geochim. Cosmochim. Acta* **62**, 2369–2387.

Moskovitz N. and Gaidos E. (2011) Differentiation of planetesimals and the thermal consequences of melt migration. *Meteorit. Planet. Sci.* **46**, 903–918.

Nasdala L., Hofmeister W., Norberg N., Mattinson J. M., Corfu F., Dorr W., Kamo S. L., Kennedy A. K., Kronz A., Reiners P. W., Frei D., Kosler J., Wan Y. S., Gotze J., Hager T., Kroner A. and Valley J. W. (2008) Zircon M257 – a homogeneous natural reference material for the ion microprobe U–Pb analysis of zircon. *Geostan. Geoanal. Res.* **32**, 247–265.

Nyquist L. E., Reese Y., Wiesmann H., Shih C. Y. and Takeda H. (2003) Fossil $^{26}$Al and $^{53}$Mn in the Asuka 881394 eucrite: evidence of the earliest crust on asteroid 4 Vesta. *Earth Planet. Sci. Lett.* **214**, 11–25.

Nyquist L. E., Shih C. Y. and Reese Y. D. (2008) Sm–Nd for Norite 78236 and Eucrite Y980318/433: implications for planetary and solar system processes. *Lunar Planet. Sci. Conf. XXXIX*. p. 1437.

Page F. Z., Ushikubo T., Kita N. T., Riciputi L. R. and Valley J. W. (2007) High-precision oxygen isotope analysis of pictogram samples reveals 2 μm gradients and slow diffusion in zircon. *Am. Mineral.* **92**, 1772–1775.

Palme H., Wlotzka F., Spettel B., Dreibus G. and Weber H. (1988) Camel Donga: a eucrite with high metal content. *Meteoritics* **23**, 49–57.

Prialnik D. and Podolak M. (1999) Changes in the structure of comet nuclei due to radioactive heating. *Space Sci. Rev.* **90**, 169–178.

Prialnik D., Benkhoff J. and Podolak M. (2004) Modeling the structure and activity of comet nuclei. In *Comets II* (eds. M. Festou, H. Uwe Keller and H. A. Weaver). University of Arizona Press, Tucson, pp. 359–387.

Robertson E. C. (1988) *Thermal Properties of Rocks*. U.S. Geological Survey, Reston.

Roszjar J., Whitehouse M. J., Srinivasan G., Mezger K. and Bischoff A. (2012) Evidence for prolonged magmatism on vesta inferred from eucrite zircon grains. *Meteorit. Planet. Sci.* **47**, A332 (abstr.).

Russell C. T., Raymond C. A., Coradini A., McSween H. Y., Zuber M. T., Nathues A., De Sanctis M. C., Jaumann R., Konopliv A. S., Preusker F., Asmar S. W., Park R. S., Gaskell R., Keller H. U., Mottola S., Roatsch T., Scully J. E. C., Smith D. E., Tricarico P., Toplis M. J., Christensen U. R., Feldman W. C., Lawrence D. J., McCoy T. J., Prettyman T. H., Reedy R. C., Sykes M. E. and Titus T. N. (2012) Dawn at Vesta: testing the protoplanetary paradigm. *Science* **336**, 684–686.

Schiller M., Baker J. A. and Bizzarro M. (2010) $^{26}$Al–$^{26}$Mg dating of asteroidal magmatism in the young Solar System. *Geochim. Cosmochim. Acta* **74**, 4844–4864.

Schuhmacher M., Chambost E. D., McKeegan K. D., Harrison T. M. and Migeon H. N. (1994) In situ U/Pb dating of zircon with the Cameca IMS 1270. In *Proceedings of the 11th SIMS Conference*. pp. 919–922.

Schmitt A. K., Chamberlain K. R., Swapp S. M. and Harrison T. M. (2010) In situ U–Pb dating of micro-baddeleyite by secondary ion mass spectrometry. *Chem. Geol.* **269**, 386–395.

Shukolyukov A. and Begemann F. (1996a) Pu–Xe dating of eucrites. *Geochim. Cosmochim. Acta* **60**, 2453–2471.

Shukolyukov A. and Begemann F. (1996b) Cosmogenic and fissiogenic noble gases and $^{81}$Kr–Kr exposure age clusters of eucrites. *Meteorit. Planet. Sci.* **31**, 60–72.

Srinivasan G., Goswami J. N. and Bhandari N. (1999) $^{26}$Al in eucrite Piplia Kalan: plausible heat source and formation chronology. *Science* **284**, 1348–1350.

Srinivasan G., Whitehouse M. J., Weber I. and Yamaguchi A. (2004) U–Pb and Hf–W chronometry of zircons from eucrite A881467. *Lunar Planet. Sci. Conf. XXXV*. p. 1709 (abstr.).

Srinivasan G., Whitehouse M. J., Weber I. and Yamaguchi A. (2007) The crystallization age of eucrite zircon. *Science* **317**, 345–347.

Stacey J. S. and Kramers J. D. (1975) Approximation of terrestrial lead isotope evolution by a two-stage model. *Earth Planet. Sci. Lett.* **26**, 207–221.

Stern R. A., Fletcher I. R., Rasmussen B., McMaughton N. J. and Griffin B. J. (2005) Ion microprobe (NanoSIMS 50) Pb-isotope geochronology at <5 μm scale. *Int. J. Mass Spectrom.* **244**, 125–134.

Strom R. G., Malhotra R., Ito T., Yoshida F. and Kring D. A. (2005) The origin of planetary impactors in the inner solar system. *Science* **309**, 1847–1850.

Tatsumoto M., Knight R. J. and Allegre C. J. (1973) Time difference in the formation of meteorites as determined from the ratio of lead-207 to lead-206. *Science* **180**, 1279–1283.

Tera F., Papanastassiou D. A. and Wasserburg G. J. (1974) Isotopic evidence for a terminal lunar cataclysm. *Earth Planet. Sci. Lett.* **22**, 1–21.

Tera F., Carlson R. W. and Boctor N. Z. (1997) Radiometric ages of basaltic achondrites and their relation to the early history of solar system. *Geochim. Cosmochim. Acta* **61**, 1713–1731.

Touboul M., Kleine T. and Bourdon B. (2008) Hf–W systematics of cumulate eucrites and the chronology of the eucrite parent body. *Lunar Planet. Sci. Conf. XXXIX*. p. 2336 (abstr.).

Trinquier A., Birck J. L., Allègre C. J., Gopel C. and Ulfbeck D. (2008) $^{53}$Mn–$^{53}$Cr systematics of the early Solar System revisited. *Geochim. Cosmochim. Acta* **72**, 5146–5163.

Unruh D. M., Nakamura N. and Tatsumoto M. (1977) History of Pasamonte achondrite – relative susceptibility of Sm–Nd, Rb–Sr, and U–Pb systems to metamorphic events. *Earth Planet. Sci. Lett.* **37**, 1–12.

Wadhwa M. and Lugmair G. W. (1995) Sm–Nd systematics of the Eucrite Chervony Kut. *Lunar Planet. Sci. Conf. XXVI*. pp. 1453–1454.

Wadhwa M. and Lugmair G. W. (1996) Age of the eurites "Caldera" from convergence of long-lived and short-lived chronometers. *Geochim. Cosmochim. Acta* **60**, 4889–4893.

Wadhwa M., Amelin Y., Bogdanovski O., Shukolyukov A., Lugmair G. W. and Janney P. (2009) Ancient relative and absolute ages for a basaltic meteorite: implications for time-

Author's personal copy



scales of planetesimal accretion and differentiation. *Geochim. Cosmochim. Acta* **73**, 5189–5201.

Wilson L., Goodrich C. A. and Van Orman J. A. (2008) Thermal evolution and physics of melt extraction on the ureilites parent body. *Geochim. Cosmochim. Acta.* **72**, 6154–6176.

Wu F. Y., Yang Y. H., Mitchell R. H., Bellatreccia F., Li Q. L. and Zhao Z. F. (2010) In situ U–Pb and Nd–Hf–(Sr) isotopic investigations of zirconolite and calzirtite. *Chem. Geol.* **277**, 178–195.

Yin Q. Z., Jacobsen S. B., Yamashita K., Blichert-Toft J., Télouk P. and Albarède F. (2002) A short timescale for terrestrial planet formation form Hf–W chronometry of meteorites. *Nature* **418**, 949–951.

Zhou Q., Yin Q. Z., Bottke B., Claeys P., Li X. H., Wu F. Y., Li Q. L., Liu Y. and Tang G. Q. (2011) Early basaltic volcanism and late heavy bombardment on Vesta: U–Pb ages of small zircons and phosphates in eucrites. *Lunar Planet. Sci. Conf. XLII*. p. 2575.

*Associate editor:* Janne Blichert-Toft